This is a non-peer reviewed preprint for posting to EarthArXiv.
The manuscript has been submitted to Frontiers in Earth Science and is in the review process at the date of posting.

Title: The influence of fluid inclusions, organics, and calcite fabric on trace element distributions in stalagmites

Authors: O. Kost1, J. Sliwinski2, N. Gies3, 1 M. Lueder3, H. Stoll1*

2 1Geological Institute; ETH Zürich, Sonneggstrasse 5, 8092 Zurich, Switzerland
3 2School of Earth and Environmental Sciences, University of St Andrews, Queen's Terrace, KY16
4 9AJ, Scotland
5 3Institute of Geological Sciences, University of Bern, Baltzerstrasse 1+3, 3012 Bern, Switzerland
6 * Correspondence:
7 Corresponding Author
8 heather.stoll@erdw.ethz.ch

# The influence of fluid inclusions, organics, and calcite fabric on trace element distributions in stalagmites

**O. Kost[1], J. Sliwinski[2], N. Gies[3], M. Lueder[3], H. Stoll[1*]**

[1]Geological Institute; ETH Zürich, Sonneggstrasse 5, 8092 Zurich, Switzerland

[2]School of Earth and Environmental Sciences, University of St Andrews, Queen's Terrace, KY16 9AJ, Scotland

[3]Institute of Geological Sciences, University of Bern, Baltzerstrasse 1+3, 3012 Bern, Switzerland

*** Correspondence:**
Corresponding Author
heather.stoll@erdw.ethz.ch

**Keywords: FTIR mapping, CLSM, LA-ICP-MS, fluid inclusions, stalagmites, trace element incorporation, calcite**

In review

**Highlights:**

- **In situ FTIR analysis in stalagmites distinguishes free water from organic matter**
- **Free water is present throughout stalagmite calcite (often) without visible fluid inclusions**
- **Na concentration can be controlled by fluid inclusions in some but not all stalagmites**
- **$K_{Sr}$ and $K_{Mg}$ agree with literature, while $K_{Na}$ and $K_U$ are highly variable**
- **Diagenetic sealing of crystallites may explain lateral chemical variations**

## Abstract

Growing stalagmites entrap water and organic molecules while incorporating trace elements in diverse crystallographic fabrics. However, the interrelationships between crystal defects, fluid inclusions, organic carbon incorporation, and trace element incorporation in stalagmites remain poorly constrained. Here we use for the first time Fourier Transformation Infrared Focal-Plane Array (FTIR-FPA) imaging to show the distribution of molecular water (3400 $cm^{-1}$ absorbance) and organic matter (2983 $cm^{-1}$) in calcite from recently grown stalagmites with known drip water hydrochemistry and one fossil stalagmite. To test if entrapped water in speleothem calcite affects the abundance or distribution of trace elements, the element distribution (Na, Mg, Sr, U, Al, Y and Zn) is mapped by Laser Ablation Inductively Coupled Plasma Mass Spectrometry (LA-ICP-MS). Transmitted Light (TL) Microscope imaging constrains crystal fabrics and displays visible features such as crystallites, crystal defects like fractures, pores or at small scale fluid inclusions, as well as detrital clays. We find that stalagmite areas with strong Organic Matter fluorescence (FOM) via Confocal Laser Scanning Microscopy (CLSM) coincide with areas of high FTIR absorbance at 2983 $cm^{-1}$, suggesting common co-location of multiple organic matter types in the stalagmite. While microscopic fluid inclusions visible in transmitted light are also detected by FTIR 3400 $cm^{-1}$ absorbance, the FTIR additionally detects in some samples abundant water in submicroscopic fluid inclusions detected by FTIR

3400 $cm^{-1}$ absorbance, but not evident in transmitted light microscopy. In most samples, Na concentration is elevated in regions of high fluid inclusion density, suggesting that a significant portion of Na may be hosted in entrapped water rather than in the calcite, consistent with the very low partitioning coefficient of Na in calcite. Only samples forming under extremely rapid drips, with 100-fold higher Y than other samples, feature Na concentrations which appear dominated by coupled Y-Na substitution and little influenced by FI Na. Our analysis provides new evidence of the influence of fluid inclusions on trace element content of stalagmites and illustrates the utility of several non-destructive imaging techniques to improve interpretations of proxy signals based on trace elements.

## 1 Introduction

Speleothems provide a time-resolved archive for past conditions. Environmental changes outside and within the cave may be recorded in geochemical proxies such as stable isotopes and trace elements in the calcite, oxygen and hydrogen isotopic ratio and noble gas content of fluid inclusions, and variations in organic biomarkers. At the same time, environmental conditions are suspected to influence as well as physical properties such as fluorescence, layer thickness, fabrics.

There is growing awareness that the final geochemical composition of speleothems can result from an interplay between calcite growth mechanisms, the dripwater chemistry, and the cave environmental setting. Elucidating the role of these processes has been complex. While calcite growth mechanisms have been studied in situ via Atomic Force Microscopy (e.g. Renard et al., 2013), similar work has not been undertaken for cave-analogue precipitation conditions. Evidence of non-classical crystallization pathways involving metastable intermediates has been observed in a few cave systems (Demény et al., 2016), but many sample collection and storage practices could accelerate transformation to more stable phases, leaving precursor phases undetected. Thus, observation of final speleothem fabrics remains an important approach to evaluate the relationships between crystallite size, orientation, and porosity and the geochemical indicators even when growth mechanism cannot be independently confirmed (Chiarini et al., 2017).

In this study, we employ a novel technique to map at high resolution the distribution of molecular water and OH as well as certain groups of aliphatic organic molecules in stalagmites using Fourier Transformation Infrared (FTIR) microscopy. We combine these new maps with detailed petrographic characterization of calcite fabrics in thin section and confocal microscopy (fluorescence), as well as laser ablation maps of the distribution of Sr, Mg, U, Y, Zn, and Na in the studied area. We focus on a set of actively growing stalagmites for which modern dripwater chemistry is known from a 16 month monitoring study (Kost et al., 2022), and map areas representing decades of recent growth. We use this set of core observations to constrain current hypotheses about the relationships between crystal defects and fluid inclusions, organic carbon incorporation, and trace element incorporation in stalagmites.

While fluid inclusions in speleothems are now widely recognized in speleothems and are analyzed for water oxygen and hydrogen isotopes and noble gases (Ghadiri et al., 2018, Affolter et al., 2014) or are used as paleothermometers (Meckler et al., 2015, Krüger et al., 2011), the controls on the distribution of water in stalagmites at both the microscopic and sub-microscopic scale has not been evaluated previously. Therefore, we seek to evaluate if there are relationships between the fluid inclusion abundance and crystallite distribution and whether fluid inclusions are more prevalent in organic rich or organic-poor areas of the speleothems.

In review



This is a provisional file, not the final typeset article

Organic chelating complexes enhance the mobility of insoluble elements to be transported to the stalagmites as discussed by Hartland et al. (2014), and to first order, many organic molecules are incorporated in calcite in proportion to their abundance in dripwater (Pearson et al., 2020a). The role of organic ligands on the incorporation of transition metals in calcite has been evaluated experimentally (e.g. Lindeman et al., 2022). We therefore assess whether organics and colloidally delivered elements follow similar spatial distribution patterns in the stalagmites.

Finally, we evaluate the relationship between non-colloidally transported trace elements, and the distribution of organics, defects, and fluid inclusions, addressing monovalent Na as well as divalent Sr and Mg. In addition to the direct substitution for $Ca^{2+}$, trace elements may be incorporated at interstitial sites (Ishikawa and Ichikuni, 1984) or crystal lattice defects (Busenberg and Plummer, 1985), or by sorption to an existing mineral surface (Curti, 1997, Paquette and Reeder, 1995, Rimstidt et al., 1998), and therefore exploration of the relationship between fabrics and element concentration may elucidate the effective controls on partitioning. A key question to date sparsely addressed, is whether submicroscopic fluid inclusions might affect trace element distributions in calcite. Elements with the lowest partitioning coefficients in calcite, such as Na, would be most strongly affected by trapped fluid phases in the calcite since the largest portion of the element remains in the liquid phase. Intersection of a fluid inclusion by laser ablation sampling or micromilling could contribute significantly to the total measured concentration of such an element. Sliwinski and Stoll (2021) and Borsato et al. (2007) hypothesized invisible submicroscopic fluid inclusions might affect trace element distributions in calcite but did not assess this mechanism. The combination of FTIR maps of water distribution with LA-ICP-MS maps of Na concentrations allows us to test this hypothesis.

As in previous studies, we examine a set of actively growing stalagmites from La Vallina Cave on the northern Iberian coast, where coeval dripwater chemistry has been measured monthly for 16 months (Kost et al., 2022). The same samples have been investigated in other studies (Sliwinski et al., 2023). Additionally, we examine one fossil stalagmite from the same cave. Due to its location only 2.5 km from the Atlantic Ocean, the cave dripwater has detectable Na in the 5 to 10 $\mu g\ g^{-1}$ range, attributed to marine aerosol deposition in the land surface above the cave (Kost and Stoll, 2023). Measuring the change of marine originating elements in stalagmites might reveal changes in wind intensity since marine aerosol delivery is controlled by wind. However, the proxy interpretation of Na requires a clear understanding of whether it is mostly hosted in stalagmite fluid inclusions or whether it partitions into calcite. We use LA-ICP-MS to compare the distribution of Na and other elements with the distribution of fluid inclusions and assess if there is significant contribution of fluid inclusions or organics to the bulk trace element content of the stalagmite for any elements.

## 2 Methods

### 2.1 Samples

In total 3 actively growing stalagmite chips (MR, PG and SS) were sampled by chipping and sawing off a small part at the top of the growth surface. Active growth was confirmed by detection of the $^{14}C$ bomb spike which also constrains average growth rates over the last several decades (Sliwinski et al., 2023). In addition, we examine the sample GLA, a fossil stalagmite with a hiatus and clear optical difference below and above the hiatus ("milky" and "glassy" calcite respectively). Previous XRD confirms that all samples are exclusively calcite.

The samples cover a range of different growth rates from 3 µm/yr (GLA) to 150 µm/yr (MR) (Table 1). The active samples span a range of drip rates and modeled growth seasonality, from only a single growth

In review

season (PG), to growth during both summer and winter but growth cessation during fall and spring (SS) (Kost et al., 2022). While the MR dripwater was not monitored for a full year and we cannot definitively infer its growth season, the cave ventilation in that sector is more similar to SS and it thus potentially records multiple growth seasons yearly. MR derives from the lower gallery with an active cave stream which periodically floods adjacent terraces. Additionally, active samples span a range of dripwater chemistries, from high Mg/Ca and U/Ca (PG) to lower Mg/Ca and Sr/Ca (SS) (Kost et al., 2022). Since GLA is a fossil stalagmite, dripwater chemistry and growth seasonality are not independently constrained, but its location in the cave was nearest SS.

The samples were cut in quarter sections and prepared as a double side polished 500 µm thick sections for the following set of analyses. To assess the addressed research questions a set of methods are applied to get the necessary information about the fluid inclusion distribution and other crystal features affecting trace element distribution (Fig. S2).

### 2.2 Digital microscope imaging

Transmitted light (TL) images were taken with the Keyence VHX-6000 digital microscope at ETH Zurich to reveal layering, calcite fabric including macroscopic FI's (Chiarini et al., 2017, Frisia, 2015) and detrital particles. Water filled FI's appear clear and bright under the microscope, whereas empty FI's appear black due to refractive effects. The presented microscope images are scans through the whole thick section providing a focused image of all depth levels (sequential focal plane). Hence, visible features such as fluid inclusions can be deep in the sample or at the surface. This is necessary for comparison with the fluid content maps (FTIR- images). Images taken with the analyzer using a cross polarizer show individual crystallites with different extinction angles, illustrating crystal boundaries or crystal zoning.

### 2.3 Confocal Laser Scanning Microscopy (CLSM)

Fluorescence maps were generated with CLSM at the Scientific Center for Optical and Electron Microscopy (ScopeM) at ETH Zurich using an Olympus Fluoview 3000. A 488 nm laser was used for excitation of the sample by detecting the fluorescence in a window of 490-555 nm. To produce a map automatic stitching of two averaged 1024x1024 pixels frames at 100x magnification was automatically performed by the microscope control software (CellSens). This technique is explained in more detail in Sliwinski and Stoll (2021). Fluorescence is generally attributed to the presence of fluorescent organic compounds. However, CLSM maps may also be disrupted by refractive effects in a few regions where the surface is open due to defects or voids. The CLSM images further help to distinguish between crystal defects within the 500 µm section (spotted in TL images but not visible by CLSM) and defects situated at the very surface where the laser maps are ablated. Refractive effects in the focal plane (sample surface) result in higher fluorescence, but in a characteristic fashion that makes them easy to distinguish from true fluorescence. Crystal defects seen in the TL image but not visible in the CSLM image are not situated at the top of the sample, hence should not affect LA-maps.

The fluorescence from the applied CLSM method is commonly interpreted as a first order indication of the concentration of OM in a region of the stalagmite (Sliwinski and Stoll, 2021), although the single wavelength excitation (488nm) and a narrow detection window of 490-555 nm are sensitive to only a narrow range of compounds and therefore may not capture all OM in stalagmites (Sliwinski and Stoll, 2021).

### 2.4 Fourier Transformation Infrared Focal-Plane Array (FTIR-FPA) imaging


This is a provisional file, not the final typeset article

Transmission FPA-FTIR spectroscopy maps were acquired at University of Bern using a Bruker Tensor II spectrometer with a globar infrared source, equipped with a Bruker Hyperion 3000 microscope. The closed Plexiglas chamber was purged with dried air during measurements to limit the interference of environmental $CO_2$ and $H_2O$ on measurements. Data was collected with a focal plane array (FPA) detector, composed of 64x64 liquid nitrogen cooled mercury cadmium telluride (MCT) detector elements on a square array in a wavenumber range of 900–4000 $cm^{-1}$ with a resolution of 8 $cm^{-1}$ and an average over 64 scans. To improve the signal-to-noise-ratio, a binning of 4 was used, resulting in 16x16 pixel with a pixel size of 10.8x10.8 µm.

FTIR records the energy specific absorption of vibrating, bending, and stretching atomic bonds caused by radiation passing through the sample. The absorbance of molecular $H_2O$ and OH creates a characteristic broadband peak located at wavenumber 3400 $cm^{-1}$(Stünitz et al., 2017). Additional absorbance at wavenumber of~2900 $cm^{-1}$ is due to aliphatic C-H stretching in organic components with -$CH_2$ and -$CH_3$ groups. In lower wavenumbers, organic components at 1540 to 1640 $cm^{-1}$ due to aromatic C=C double bonds and H bonded to C=O, and 1370 to 1430 $cm^{-1}$ due to COO- symmetric stretching, may overlap with the asymmetric stretch vibration of the $CO_3$ group in the 1400-1500 $cm^{-1}$ range (Lebron and Suarez, 1996). The most commonly described organic components in stalagmites, such as lignin and its backbone, aromatics, and humic acids are all attributed to absorbances at wave numbers in the 1650 to 1265 $cm^{-1}$ range (Artz et al., 2008).

Here we present linear absorbance intensity maps from the 3400 $cm^{-1}$ band, a 2983 $cm^{-1}$ band from organics, and the linear absorbance ratio of the 3400 $cm^{-1}$ to the 2983 $cm^{-1}$ bands (Fig. 1). The latter ratio is evaluated to show the ratio of absorption of organic bonds vs $H_2O$ or OH bonds. For the data processing of the FTIR-FPA maps, the atmospheric correction and concave rubber band correction with 64 points and four iterations was performed in OPUS® version 8.5. A deconvolution of each spectrum was performed in the software package SpecXY (Gies et al., in preparation) to obtain the intensity of the water peak at 3400 $cm^{-1}$ and reduce the impact of signal noise and possible overlapping peaks present in the spectra (Fig. 1). FTIR features a linear relationship between measured linear absorbance and water/trace element content. However, the linear absorption coefficient needed for the conversion of absorbance to water content is not well defined for calcite. Thus, we conservatively report linear absorbance values for the 2983 $cm^{-1}$ and 3400 $cm^{-1}$ bands, and for the 3400 $cm^{-1}$ band, relative distribution maps are calculated by normalizing the linear absorbance to the maximum linear absorbance of each sample. Additionally, we explore a quantitative conversion of the deconvoluted 3400 $cm^{-1}$ broadband peak, employing the wavenumber specific calibration of (Paterson, 1982) to calculate quantified water maps in µg/g (ppm $H_2O$) similar to the approach of (Stünitz et al., 2017), using $\epsilon i$ factor of 1/3 as the orientation factor for uniaxial crystals(Paterson, 1982).

Laser Ablation Inductively Coupled Plasma Mass Spectrometry (LA-ICP-MS) mapping

The thick sections were glued on conventional microscope glass plates and mounted in the Laurin Technic S155 2-volume laser ablation system at ETH Zurich. A 193 nm ASI Resolution ArF excimer laser ablates in a 370 mL/min high purity He and 5.0 mL/min $N_2$ atmosphere. Ar (1.0L/min) carries the sample mixture to the Agilent 8800 Triple Quadrupole ICP-MS where it is ionized and analyzed in single quadrupole mode without reaction cell or subsequent mass filter. To obtain chemical maps, parallel lines were ablated using a 20x20 µm square spot with a scan speed of 20 µm $s^{-1}$ at an ablation rate of 10 Hz and ablation energy of 4 J $cm^{-2}$. The sampling depth is less than 10 µm (Sliwinski and Stoll, 2021). For each laser track a precleaning ablation was performed to reduce contamination. NIST- 612 was used for standardization which was performed on the Iolite 4.0

In review

208 software (Paton et al., 2011). Since NIST-612 is a synthetic glass, additional reference materials
209 (pressed carbonate powders by µ- standards: BAM RS-2-NP; ECRM-752-1*-NP; JCt-1*-NP) are
210 used in a quality check analysis (a typical example is shown in Fig. S1). Due to the matrix mismatch
211 of the NIST-612 standard and the sample (glass vs. calcite respectively) and different concentration
212 ranges for some elements (e.g. Na is orders of magnitude higher in NIST-612 compared to our
213 samples) the absolute concentrations may be biased by up to 20 % as examined by the quality check
214 analysis (Fig. S1). Nevertheless, qualitative interpretation of differences within and between samples
215 is reasonable since offsets (if any) would be constant. We report element concentrations and
216 additionally calculate trace element to Ca ratios normalizing to 40% Ca in the measured solid. We do
217 not show data for any point in which Ca counts per second (CPS) were < 800'000 to avoid mapping
218 open voids, pores and fractures. For subsequent evaluation of trace elements controlled by processes
219 other than the presence of detrital clays, we apply a filter with a cutoff of >6 ppm Al (Fig. S1).

220 **2.5 Spatial Referencing and map visualization**

221 The presented maps were aligned manually by visual fitting using Adobe Illustrator 2023. Prominent
222 features visible in all produced images (cracks, edges, pores, layers etc.) were used to reference the
223 different images.

224 The IR absorbance is integrated over the whole 500 µm thick section, and it therefore does not give
225 any information about the depth where the water is situated. While this is consistent with the
226 detection of FI's by transmitted light microscopy (where sequential focal planes are added together),
227 it may be at odds with CLSM and LA-ICP-MS data, which are both sampled from the uppermost
228 ~10 µm of the surface. One challenge is that FTIR-maps and TL images visualize FI's throughout the
229 whole 500 µm section, however, LA-maps record <10 µm at the surface where potential FI's could be
230 ruptured and lose fluid during sample preparation and therefore the true FI influence may be
231 underestimated by LA scans. Within this 10 µm depth of the ablation, larger pores of dimension 10
232 µm or larger are more likely to intersect the surface and be exposed during polishing and potentially
233 opened, whereas some fraction of smaller <2 µm pores are more likely to remain intact and closed
234 within that ablation depth range. Thus, the discrepancy between LA scans and FI estimates would be
235 most significant for the larger fluid inclusions of similar dimension as the depth ablation crater.

236 **3 Results**

237 **3.1 Calcite fabrics and fluorescence**

238 **3.1.1 Calcite fabrics**

239 The rapidly growing active stalagmites (SS1, SS2, MR1 and PG2) are all comprised of porous
240 columnar microcrystalline (Pcm; according to Chiarini et al., 2017) calcite fabric and appear
241 generally milky with a detailed region of study which is encompassed within a single crystallite (or
242 two crystallites in case of SS2) (Fig. S2). In contrast, the order of magnitude slower growing fossil
243 stalagmite (GLA) is composed of columnar and columnar open (C & Co) fabrics with very clear
244 compact columnar calcite, in which the area of interest spans several crystallites of varying extinction
245 angle and crystallites are smaller than in the rapidly growing active stalagmites. A new set of
246 crystallites is established in GLA above the prominent detrital layer of the hiatus.

247 **3.1.2 Organic distribution in fluorescence and FTIR at 2983 $cm^{-1}$**

248 In samples with a strong CLSM fluorescence signal, the intensity of FTIR absorbance at 2983 $cm^{-1}$,
249 attributed to aliphatic C-H stretching in organic components, exhibits a generally similar spatial

In review



This is a provisional file, not the final typeset article

distribution as fluorescence (Fig. 2-6). In SS2, areas of higher CLSM fluorescence are also higher in 2983 $cm^{-1}$ absorbance (Fig. 3). In SS1, narrow low fluorescence bands perpendicular to growth layers are also low in 2983 $cm^{-1}$ absorbance (Fig. 4). Bundles of growth layers of higher fluorescence are also high in 2983 $cm^{-1}$ absorbance, although the artifact from refraction on a defect or internal porosity in the FTIR image complicates the visualization of this contrast somewhat. The high fluorescence in the hiatus of GLA is also peak area of 2983 $cm^{-1}$ absorbance (Fig. 2). Likewise, the PG2 sample which has very limited fluorescence has a 2983 $cm^{-1}$ absorbance map dominated by grid processing issues which could be consistent with very low absolute 2983 $cm^{-1}$ absorbance (Fig. 6). In MR1, fluorescence resolved little structure in the stalagmites, because it is dominated by imperfections in the surface topography or near-surface defects causing reflection artifacts (Fig. 5). In contrast, the 2983 $cm^{-1}$ absorbance map reveals not only high concentrations in the infill of a fracture (epoxy?), but also shows variation in 2983 $cm^{-1}$ intensity among different growth layers not resolved by CLSM fluorescence. CLSM also resolves internal ruptures. In SS2, two parallel fractures crosscutting layers at intermediate angle are visible in CLSM fluorescence due to reflection (Fig. 3). Along the vertical crystallite boundary in SS2, CLSM reflection is also noted (Fig. 3).

Among the active chips, one (SS1, SS2) exhibits clear fluorescent laminations (Fig. 3, 4), whereas the other fossil and active stalagmites exhibit none. Both prepared samples, SS1 and SS2, show regular fluorescent layering (<50 µm). Comparison with the estimated growth rate over the last 60 years ($^{14}C$ bomb peak) implies subannual layering since layer spacing is mostly smaller than the estimated annual growth rate (ca. 130 µm $yr^{-1}$), although annual scale layering cannot be excluded if average growth rate were slower in the sampled intervals. Several bundles of fluorescent layers comprise super- annual banding, which is mirrored by bands of FI's.

### 3.2 Distribution of visible Fluid Inclusions and FTIR OH vibrational mode

In this study, FI are defined as small scale (<20 µm) voids filled with water embedded in calcite. Both of the techniques we employ detect FI's or $H_2O$ (FTIR) throughout the whole 500 µm section (sequential focal planes). With the resolution of our TL images, we identify readily the FI greater than about 1 µm in diameter. All examined samples contain regions with microscopic fluid inclusions visible in TL microscopy (Fig. 2-6). Active samples SS1 (Fig. 4), SS2 (Fig. 3) and MR1 (Fig. 5) show bands of higher FI density along growth layers. PG2 reveals fewer and homogeneously distributed FI's (Fig. 6). GLA features clusters of inclusions between the crystallites (Fig. 2).

The FTIR mapping technique identifies water in both visible microscopic as well as submicroscopic FI's (<<1 µm). Regions of high intensity of the 3400 $cm^{-1}$ band (O-H bonding) also feature a high linear absorbance ratio of the 3400 to 2983 $cm^{-1}$ bands (Fig. 7) as expected if spatial variations in water, rather than spatial variations in organic phases, dominated the spatial distribution of the 3400 $cm^{-1}$ band. Therefore, we compare the normalized intensity maps of the 3400 $cm^{-1}$ band with the distribution of FI and here describe both as spatial variations in water content. The normalized intensity of the 3400 $cm^{-1}$ band varies significantly, up to 5-fold, in different areas of a given sample (Fig. 3-6 and 7).

In case of PG2 the more homogenous intensity of the 3400 $cm^{-1}$ band confirms the observations made in TL images with a generally low FI density homogeneously distributed without clusters or bands of FI's as observed in the other samples (Fig 6). In MR1 and SS2, visible bands of high FI density coincide with bands of higher IR absorbance of the 3400 $cm^{-1}$ band (Fig. 3 and 5). However, even within these samples, the bands with highest FI density do not necessarily indicate highest IR absorbance of the 3400 $cm^{-1}$ band (MR1 or SS2). The amplitude of variations in water content is

In review

high, with some areas featuring 10 times less water than the maximum in MR1 (Fig. 5). Also, the size of the FI's does not seem to affect total IR absorbance of the 3400 $cm^{-1}$ band. For example, the elongated FI's along a growth-layer parallel textural discontinuity in SS2 do not yield the highest IR absorbance of the 3400 $cm^{-1}$ band in this sample; rather highest IR absorbance of the 3400 $cm^{-1}$ band coincides with other zones with finer FI's (Fig. 3). It is possible that large FI's lost part of their water either during sample preparation (cutting and polishing) or enclose air trapped during closure of the pore.

A slightly different presentation is seen in SS1 (and SS2), which shows patches of high IR absorbance of the 3400 $cm^{-1}$ band not obviously correlated with higher visible FI density, as well as FI trails along growth layers with rather low 3400 $cm^{-1}$ band absorbance (Fig. 4, 5). SS1 features smaller variations with a relative water content ranging only between 30 and 100% of the maximum water density. The appearance of the FTIR image looks like a honeycomb pattern. The visible FI bands in SS1 are not controlling the IR absorbance of the 3400 $cm^{-1}$ band but rather clear compact calcite with low visible FI density reveals high IR absorbance suggesting water in compact calcite (Fig. 4). Consequently, the normalized intensity map of the of the 3400 $cm^{-1}$ band suggests water where it is not expected from the visual FI distribution.

From both normalized intensity maps of the 3400 cm-1 band and TL, high water concentrations are observed in GLA along the hiatus, 10 times higher than the minimum (Fig. 2). The elevated IR absorbance fingers above the hiatus coincide with higher visible FI density and often follow crystallite boundaries (Fig. 2). The quantification of water content (Supplementary Figure S4, Supplementary text 1.2) suggests water contents in the range of 0.05 to 0.25% in most samples.

### 3.3 Distribution of detrital clays and associated elemental enrichment in hiatus, pores and fractures

All of our samples show the presence of detrital particles in TL microscopy, and these correspond with regions of very high Al content in LA-ICP-MS maps (Figure S1). Al shows a bimodal distribution, with high Al zones reaching 10-20 ppm at maximum and concentrations in the visibly cleaner calcite closer to 1 ppm.

Detrital minerals are concentrated in the hiatus, along fractures, and in pores. The most prominent detrital contributions are recorded in GLA which represents a hiatus spanning thousands of years (Fig. S1). In GLA, detrital layers occur only along this hiatus horizon and just below it in infilled defects. In SS2 there are distinct layers of detrital enrichment marked by high Al content and detrital particles in TL; one such layer coincides with a change in calcite fabric and appears to represent a discontinuity in growth conditions (Fig. S1). MR1 features a layer of enriched Al along the fracture, and also in some layers in the lower portion of the sample which coincide with FI-rich bands. Detrital enrichment in fractures is also seen in PG2 (in growth direction and opening into pore, Figure S1) and SS2 (fissure fracture within crystallite seen Fig. S1). In contrast, the fracture along the crystal boundary detected in SS2 or the fracture in SS1 (Fig. S1) is not very prominent in Al (no detrital contamination, hence fracture likely originates from sample preparation). Furthermore, detrital particles and Al enrichment are noted in inter- and intra-crystalline pores.

### 3.4 Average element concentrations in detrital-free calcite

In review



This is a provisional file, not the final typeset article

### 3.4.1 Average composition and trace element partitioning

The average composition of the stalagmites differs significantly in some elements (Fig 8). Mg concentration is nearly 10-fold higher in GLA and PG2 than in SS1, SS2 and MR1. U concentration in PG2 is nearly 10-fold higher than in other stalagmites. Y concentration in SS1 and SS2 is 10-fold higher than PG2 and 100-fold higher than GLA and MR1. Average Sr concentrations are similar among most stalagmites but about 2-fold higher in PG2. Mean Na concentrations are similarly high in SS1, SS2, and PG2, but 2-fold lower in MR1, and 5-fold lower in GLA.

For actively growing stalagmites with monitored dripwater chemistry, average incorporation coefficients were calculated for the mean stalagmite concentration (Fig. 9). This calculation assumes that the range in dripwater chemistries over the 16-month monitoring period at each site is representative of dripwater chemistry at that site over the several decades period of growth integrated in the average LA-ICP-MS map. This calculation also assumes that the stalagmite growth depletes only a small fraction of the precipitable Ca in the dripwater (e.g. maintain a high Rayleigh f) so that dripwater does not evolve significantly during the deposition interval. If this latter assumption is not sustained, then we could overestimate the partitioning coefficients in proportion to the degree of Ca depletion. Based on these assumptions, the range in Sr and Mg partitioning coefficients is within the ranges reported in previous publications (Tremaine and Froelich, 2013 and references in their Table 4). Sr partitioning is slightly higher in the high Mg PG2 compared to other samples. U partitioning varies over a greater range than previous reports (Day and Henderson, 2013), with our estimates including samples both higher (SS2) and lower (MR1) than published range. Inferred Na partitioning is similar to previous estimates in PG2 and MR1. However, for SS1 and SS2 (same stalagmite sample), the calculated effective stalagmite partitioning coefficients are more than twice as high as the highest endmember $D_{Na}$ ($1.3*10^{-3}$) derived by Füger et al. (2019) and several orders of magnitude higher than the $D_{Na}$ derived by Devriendt et al. (2021).

### 3.4.2 Spatial distribution of Sr, Mg, Na, Y, U, and Zn

Spatial variations are pronounced for most elements (Fig. 10-14). Alternations of Y content among growth layers on 60-150 μm length scale is evident for SS2, PG2, and SS1 (Fig. 11, 12 and 14). Comparison with the estimated growth rate implies this could be annual scale layering, especially in SS1 if its growth rate in the imaged section were faster than average (Table 1).

At longer timescale, variations in other elements occur among growth layers in some of the actively growing samples as well as GLA. For example, SS1 (Fig. 12) and SS2 (Fig. 11) show distinct variations between growth layers in Mg, Sr, Y and weaker signal variations in U and Zn. Growth layers do not show a consistent relationship of elemental covariation, for example in the upper part of SS2, Y has strong variation but Sr is more stable. Yet, in the lower half of this sample Y show up to 5-fold changes and clear inverse correlation with Sr (less than 2-fold range). PG2 (Fig. 14) has no significant variation among growth layers, with the exception of Y. MR1 (Fig. 13) features some high frequency Y variations, which do not appear to be annual, and weak variation in Sr and U. Water and defect-rich growth layers are not correlated with unusually high or low concentrations of Mg, Sr, or U in MR1, PG1, SS1 or SS2 (Fig. 11-14).

In all samples except PG2, there is elemental variation perpendicular to growth layers. In SS1 (Fig. 12) and SS2 (Fig. 11), these are narrow zones crosscutting annual growth layers, which are lower in Sr, U, and Y, and lower in fluorescence. The narrow zones are also lower in water content in SS1. Many of these features are visible in TL images as dark zones, which in the visual image appear to be defects. In contrast, the broad portions of the growth layer between these crosscutting features reveals

In review

clearer calcite, elevated Sr and brighter fluorescence. In GLA (Fig. 10), above the hiatus the crosscutting features coincide with the boundaries among crystallites, and affect U and Na strongly (enrichment), but also affect Sr and Y (depletion).

# 4 Discussion

## 4.1 Evaluation of methods for mapping the spatial distribution of water and organics in stalagmites

While FTIR has been employed previously on aggregate stalagmite samples or decarbonated stalagmite powder (Gázquez et al., 2012, Martínez-Pillado et al., 2020), the present study illustrates the novel application of FTIR microscopy to map the spatial distribution of water (3400 $cm^{-1}$ band) and organic molecules (2983 $cm^{-1}$ band) in a speleothem section.

For the detection of organics, one advantage of FTIR spectroscopy is that it is less sensitive to the topography of the polished stalagmite surface and near-surface reflection effects compared to CLSM, as observed in our sample MR1 (Fig. 5). Although not exploited here, the technique could have the potential to distinguish an array of organic components through full deconvolution of the organic peaks in the in the 1650 to 1265 $cm^{-1}$ wavenumber range, as completed for analysis of peat samples (Artz et al., 2008). This contrasts with standard CLSM which typically uses a narrow excitation/emission pair.

In this study, CLSM was limited to detecting organic components excited at 488 nm and fluorescing in the window of 490-555 nm, a small fraction of the total fluorescent organic constituents delivered to speleothems in this cave (Endres et al., in review), and potentially emphasizing components such as lignin (Sliwinski and Stoll, 2021). From FTIR, we focused on the 2983 $cm^{-1}$ band of the asymmetric $CH_2$ component which is expected in fats, waxes, and lipids. Our initial, qualitative comparison of CLSM and the FTIR 2983 $cm^{-1}$ band suggests that they are generally elevated in the same regions of the speleothems, although they likely target differing classes of organic material. One explanation is that various classes of organic components are co-located in the same zones of the stalagmite, i.e. bands high in lignin are also high in lipids and waxes. Future studies in precisely co-referenced maps could quantitatively compare the intensity variations of the 2983 $cm^{-1}$ band and other FTIR organic bands in the 1650 to 1265 $cm^{-1}$ wavenumber range with the CLSM fluorescence maps.

For the detection of water, one advantage of FTIR spectroscopy is that it has the potential to detect submicroscopic FI smaller than can be resolved by standard transmitted TL microscopy. Indeed, we find that through the 3400 $cm^{-1}$ band, it is possible to detect zones with high density of microscopic FI but also identify high water content in areas where no microscopic FI were recognized (e.g. SS1; Fig. 4). Additionally, the linear absorbance readily quantifies the scale of changes in water abundance in different regions of the sample.

One challenge with FTIR microscopy is that the 3400 cm-1 band detects OH which may be present as free water (e.g. in fluid inclusions), as interstitial $H_2O$ in the crystal lattice or as OH groups bound to organic molecules (and other phases). In previous FTIR application on bulk samples, the 3400 $cm^{-1}$ band is routinely attributed to water in biominerals (Engin et al., 2006) but in abiogenic minerals it is commonly attributed to OH groups in organic compounds (Gázquez et al., 2012). Here, to compare the distribution of the OH peak with organic components, we also quantified the distribution of an organic-attributed band (2983 $cm^{-1}$). Because of the interference of the $CO_3$ group in the region of the most commonly described organic components of stalagmites in the 1650 to 1265 $cm^{-1}$ wavenumber

In review



This is a provisional file, not the final typeset article

range (Artz et al., 2008, Martínez-Pillado et al., 2020), we focused on the linear absorbance of the 2983 $cm^{-1}$ band of the asymmetric $CH_2$ component which is expected in fats, waxes, and lipids.

As a first order qualitative test of whether sectors of the stalagmite high in 3400 $cm^{-1}$ band linear absorbance were only located in areas of high abundance of organics, we mapped the ratio of the 3400 $cm^{-1}$ band linear absorbance to 2983 $cm^{-1}$ band linear absorbance. If all elevated 3400 $cm^{-1}$ band linear absorbance were proportionally due to elevated 2983 $cm^{-1}$ band, then this ratio would be constant spatially across the stalagmite. Yet, we observe that regions of high 3400 $cm^{-1}$ band linear absorbance are also characterized by a high 3400 $cm^{-1}$ band to 2983 $cm^{-1}$ band ratio, implying increased OH stretching relative to $CH_2$ stretching of aliphatics. We have interpreted this as evidence that a significant portion of the 3400 $cm^{-1}$ band linear absorbance signal reflects free water. This interpretation assumes that the 2983 $cm^{-1}$ band linear absorbance is representative of the abundance distribution of the broad suite of organic components which could feature OH groups. In future work, such an interpretation could be more rigorously tested by a full deconvolution of the organic peaks in the in the 1650 to 1265 $cm^{-1}$ wavenumber range.

## 4.2 Effects of variable organic distribution in stalagmites

### 4.2.1 Is the FI and defect density higher in organic rich growth layers?

Because greater concentrations of dissolved organic matter (DOM) in dripwaters translate to greater concentrations of OM in stalagmites (Chalmin et al., 2013, Pearson et al., 2020b), layers of higher abundance of organic components in the stalagmite may reflect times of higher dripwater DOM delivery. Experimental calcite precipitation at varying concentrations of dissolved organic matter types typical of karst dripwaters, showed significant effects of OM incorporation on calcite fabric (Pearson et al., 2020b). Compared to no DOM, the low DOM experiments featured more rounded rhombohedral corners and higher density of micron to sub-micron kinks which may represent active sites of DOM adsorption. The higher DOM experiments featured chiral rhombohedral morphology and elongation of the longest axis of crystals, and corners and pits with high step density and a larger number of pores. Greater density of pores may further enhance the concentration of OM in the stalagmite. These laboratory results are consistent with prior description that due to the incorporation of OM into the calcite lattice, more crystal defects (on sub-microscopic scale) are expected (Phillips et al., 2016, Green et al., 2016).

However, in the samples examined here, we find that growth layers with greater density of FI and of high 3400 $cm^{-1}$ band linear absorbance coincide with low fluorescence (e.g. SS1, SS2 and MR1; Fig. 3-5). The fluorescent layering disappears in FI bands (especially elongated FIs) suggesting low organic incorporation in those zones contrasting with higher organic concentrations in compact calcite (i.e. discontinuity in SS2; Fig. 3). Similarly, the CLSM images often show low fluorescence in disturbed calcite fabrics, suggesting low organic content in these fabrics. Across the different examined growth layers, the range of organic contents evident from fluorescence and 2983 $cm^{-1}$ band linear absorbance may not encompass a wide enough variation in DOM content to significantly alter the growth mechanisms and fabrics.

### 4.2.2 What is the relationship of organics and colloidally delivered elements?

Some previous studies have documented a close spatial correspondence between fluorescence and elements such as Y, Zn and some other transition metals, a correlation often attributed to a colloidal transport (chelate complexes) and incorporation into calcite (e.g. Hartland et al., 2012, Rutlidge et al., 2014, Sliwinski and Stoll, 2021). In comparing the different samples examined here, we observe that the samples with higher fluorescence (SS1 and SS2) are also much higher in Y than the samples with

In review

low fluorescence (MR1, PG2 or GLA), suggesting substantially lower organic content correlates with lower Y concentrations. The same trend is revealed in Zn. One explanation is that organic compounds in dripwater may carry colloidally complexed elements such as Y and Zn (Hartland et al., 2012).

However, within an individual sample, our new results show the incorporation of both organics and colloidally transported elements into calcite to be more complex. Colloidally transported elements such as Y exhibit strongest variation among different growth layers and more limited lateral variations in our active stalagmites. Variation in dripwater chemistry or cave environmental parameters over time may contribute to these temporal variations. Yet, unlike results from slower growing fossil stalagmites from the same cave (La Vallina Cave) presented by Sliwinski and Stoll (2021), the growth layers of elevated Y and Zn of recently grown stalagmites examined here do not correlate persistently with elevated fluorescence (consistent with Sliwinski et al., 2023 investigating Y in other regions of the same samples). Rather, Y is elevated in water rich layers identified from 3400 $cm^{-1}$ band absorbance in MR1 (Fig. 13) and in SS2 (Fig. 11). In contrast, PG2 (Fig. 14) and SS1 (Fig. 12) show layers of high Y without any relationship with crystal defects or water.

We also do not see an ubiquitous covariation of Y and Zn as suggested by Chiarini et al. (2017) or Sliwinski and Stoll (2021) and described in many annually banded stalagmites (Borsato et al., 2023, Borsato et al., 2007). The correlation of Y and Zn is clear only in SS1 (Fig. 12) and SS2 (Fig. 11). Thus, more diverse delivery and incorporation mechanisms of Y and Zn appear to operate in the active growth of recent samples. Seasonal Y banding in fossil samples from this cave has been described to result from the interplay of driprate and colloid delivery and $CaCO_3$ deposition rate (Sliwinski et al., 2023). For example, colloidally transported elements may reach higher concentrations in the stalagmite in the seasons of slowest $CaCO_3$ deposition because they are subject to less dilation; the season of slowest $CaCO_3$ deposition depends on the interplay of cave and soil $pCO_2$ as well as drip rates (Sliwinski et al., 2023). Potentially, fossil stalagmites from this cave may reflect a different synchronization of ventilation, soil $CO_2$, and drip rate than occurring the last decades of growth of active stalagmites (MR, PG and SS; Fig. 11-14) under the recently changing environment. An altered seasonal ventilation regime due to rapid anthropogenic changes in exterior temperature in recent decades relative to the long-term adjustment of cave temperature, may contribute to disruption of seasonal cycles in cave ventilation and $CO_2$ which in turn affect the season of maximum and minimum $CaCO_3$ deposition.

The above conversation assumes a trace element delivery that is constant in time, either aided by colloids or fully dissolved in the dripwater. However, another mechanism contributing to element delivery to stalagmites is dry aerosol deposition, which is likely an important mechanism during growth cessation for example due to stop in drip flow. For example, block fall or strong ventilation winds can raise dust within the cave which can deposit on the stalagmite surface. We cannot distinguish if detrital elements present in pores and fractures have been transported in by drip water, or if pores accumulate and trap detritals from drip water wash in or dry aerosol deposition. However, the ever-present possibility of this manner of deposition means that the traditional soluble-colloidal division of elements cannot always be an accurate model.

### 4.3 The distribution of water in stalagmites

The formation mechanism of the pores, which may contain water, is still debated (e.g. Chiarini et al., 2017, Frisia et al., 2018). Molecular scale studies have shown growth defects deviating from the ideal spiral growth as one source of voids (De Yoreo and Vekilov, 2003). Laboratory precipitation


This is a provisional file, not the final typeset article

experiments suggested higher dripwater DOM promotes more defects and pores (Pearson et al., 2020b, Green et al., 2016, Chalmin et al., 2013), while trace element additives similarly introduce morphological deformations that may give rise to entrapped pores (Meldrum and Hyde, 2001, Wasylenki et al., 2005). Crystal defects could also be promoted by organic coating or impurities in the calcite lattice for example by clays. While it has been proposed that faster growth results in more crystal defects, Chiarini et al. (2017) suggest that more porous calcite forms at slower growth rates due to incorporation of elements inducing crystal lattice defects.

Our set of samples does not reveal a clear relationship of pores or water with average decadal-scale stalagmite growth rate defined by the bomb spike (Table 1). We do not recognize a greater number of pores or microscopic FI in the faster growing active stalagmites (MR1, SS) compared to the slower PG2. We do observe that the more homogeneously distributed FI occur in PG2, which according to monitoring precipitates calcite during a single season. In contrast, in SS and MR1 where FI's are concentrated in certain growth layers. We do not resolve a fluid rich and fluid poor alternation within each yearly increment, as seen in some studies (Wassenburg et al., 2021). It is possible that the multiple growth seasons in SS condition the formation of inclusion rich layers during some environmental conditions. However, our data do not constrain the mechanism. Because we cannot resolve growth rate differences among individual growth layers or phases, it is possible that within-sample growth rate variations do correlate with FI density.

One important observation is an enrichment of visible and elongated FI's from TL images superimposed on condensed phases of growth as revealed for example by GLA or SS2 (Fig. 2, 3). The higher IR absorbance at 3400 $cm^{-1}$ observed along hiatuses and growth discontinuities with detrital layers (GLA, SS2) is likely due to water bound to clays. At the same time, defects around the GLA hiatus, potentially triggered by detrital minerals, also coincide with visible FI indicating discrete free water regions (Fig. 2). Similarly, SS1 and SS2 do reveal a higher water content in organic rich areas (e.g. upper part in SS2; Fig. 3), which seems to be consistent with the observations of Pearson et al. (2020b) suggesting DOM to promote crystal defects. However, in SS1, areas of higher water content paradoxically coincide with the most transparent, microscopic FI and defect free calcite.

Maps of FTIR absorbance at 3400 $cm^{-1}$ also suggest regions of higher water content in stalagmites which do not coincide with microscopic fluid inclusions visible in TL images (e.g. honeycomb pattern in SS1; Fig. 4 and 12). We interpret these regions must contain submicroscopic FI's as suggested by Sliwinski and Stoll (2021), Borsato et al. (2007) and Chiarini et al. (2017). Such submicroscopic FI's undetected by TL microscopy dominate the water distribution in SS1 and PG2 and potentially influence on the distribution of the most incompatible trace elements.

In PG2, dominated by dispersed submicroscopic fluid inclusions, high water content coincides with defect-rich calcite (Fig. 6). This pattern is evident in other samples, with the exception of SS1 (low water in defects). This suggests that water remains in crystal defects or is adsorbed to the calcite surface in some crystal defects or fractures. However, in some major fractures, i.e. in SS2, the water content is low, suggesting that the stage of fracturing may affect water distribution and fractures generated during sampling or preparation do not affect water distribution. Meanwhile, some larger inter- (between crystallites) and intra-crystal pores (within crystallites) pores with visible detrital contamination do not yield higher IR absorbance in other sections (e.g. SS1, PG2; Fig. 4, 6) and may have lost their water during closure or sample preparation.

### 4.4 Do fluid inclusions increase the measured Na concentrations?

In review

The average incorporation coefficients for Na for some of our actively growing stalagmites (SS1 and SS2), using median Na of the laser maps (Fig. 9), are higher than estimated from previous experimental calcite precipitation (Füger et al., 2019). Either the laboratory determined partitioning coefficients are not representative of Na incorporation into calcite in these speleothem growth settings, and/or simple partitioning from the drip water to calcite does not account for the main process hosting Na in the speleothem calcite. Because the absolute partitioning coefficient of Na is more than an order of magnitude lower than the other measured trace elements, Na would be the element most sensitive to contribution from microscopic or sub-microscopic FI's.

The distribution of water in stalagmites suggests that FI's could control spatial variations in Na within some samples, but not others. Within SS1 and SS2, FTIR suggests water is dominantly in compact calcite in submicroscopic FI's, in which polishing during sample preparation would impart minimal disruption of FI's at the scale of laser ablation depth (<10 μm), so these very small FI's may be more likely to be intersected by the laser path and record an appreciable trace element signature. Yet, the high water enriched zones in SS1 and SS2 do not show elevated Na. This suggests that in this sample, most of the Na is hosted in the calcite lattice or interstitially (i.e., not in the fluids). Additionally, cave monitoring suggests very limited (<10%) temporal variation in the Na concentration of an individual drip over a seasonal cycle probably due to strong buffering of concentration by cation exchange in soils (Kost et al., 2022, Tadros et al., 2019). At length scales similar to annual growth increments, and laterally along the same growth increment, there are much larger (>2-fold) spatial variations in Na concentrations in stalagmites. These larger variations do not correspond to changes in the water content in most cases, and therefore likely reflect variable effective incorporation in the calcite itself. As shown by Füger et al. (2019), Na incorporation depends on growth rate. Therefore, it is possible that changes in growth rates along a growth surface can result in such lateral variations.

In contrast, in MR1, detailed imaging shows two bands of high 3400 $cm^{-1}$ band absorbance with coincident microscopic inclusions visible in TL (Fig. 13). High Na spots are more frequent within these bands and especially corresponding to defects in the TL image. In GLA, the only sample in which the studied region is comprised of multiple crystallites, the 3400 $cm^{-1}$ band absorbance suggests concentration of water between the crystallites, although visible FI in TL are not concentrated at these boundaries (Fig. 2). Where FTIR indicates water between crystallites, high Na and U concentrations occur in these boundary areas (Fig. 10). Also, in GLA (Fig. 10), very locally-distributed clusters of high FI density with twice the water absorbance are enriched in Na by a factor of 2 at the ablation surface while other high water regions do not affect Na likely because the FI's are situated deeper in the sample than the laser ablation depth.

To reconcile these observations of diverse response in MR1 and GLA vs. SS1/SS2, we propose that FI's do enrich the Na concentrations measured by LA-ICP-MS. However, this effect is more easily detectable in stalagmites with initially low calcite Na concentration. In the same way that a signal is more easily detectable when the background is low, any influence of FI's on Na concentration is more detectable against a lower baseline (perhaps due to a lower partitioning coefficient). For instance, MR1 has at least fourfold lower Na incorporation and Na concentration than SS1 and SS2. Although partitioning cannot be calculated for the fossil stalagmite GLA, due to lack of corresponding dripwater, it features the lowest average Na concentration of all stalagmites, roughly twofold lower than MR1 and fivefold lower than SS1 and SS2 (Fig. 8). In these samples, the FI's and/or the associated defects locally enhance Na. In contrast, we propose that other factors raise the background Na partitioning into calcite in SS1 and SS2 and therefore the additional Na contribution from FI's is a negligible proportion of the total measured Na. Thus, paradoxically, FI Na is not

In review



This is a provisional file, not the final typeset article

responsible for the anomalously high Na incorporation coefficients in SS1 and SS2 compared to laboratory calcite experiments (Fig. 8). If the quantitative estimates of water content, in the 0.1 to 0.25 volume % range (Supplementary Figures S4-S5, Supplementary text 1.2) are accurate, then a water-free effective partitioning Na coefficient two orders of magnitude lower in MR1, PG2, and GLA than in SS1 or SS2 would be consistent with the observed water content and bulk Na concentration. Assuming such partitioning coefficients, the spatial variation in water content in MR1 could lead to over 2 to 3-fold changes in the total (water+calcite) Na concentration of the sample. A similar magnitude spatial variation in water content would lead to only 5% and 2% spatial variations in Mg concentration in MR1 and PG2, respectively. Spatially varying water content would induce <1% variation in Sr concentrations.

The higher Na partitioning in the SS1 and SS2 calcite is not likely attributable to growth rate, since its growth rate is similar to MR1 (Table 1). SS1 and SS2 form under faster drip rates and feature much higher fluorescence, organic content as well as Y concentration. The causes of high Y concentration in this sample are detailed in (Sliwinski et al., 2023). The very high concentration of $Y^{3+}$ may increase $Na^{+}$ incorporation in order to maintain charge balance via coupled substitution (Voigt et al., 2017), potentially explaining the water-unrelated enrichment of Na in SS1 and SS2.

In caves near the coast, such as La Vallina, marine aerosol deposition in the land surface above the cave may be a significant source to Na in dripwater (Kost and Stoll, 2023). Since marine aerosol delivery is controlled by wind intensity, the Na content in dripwater may increase with past wind intensity. However, our new results suggest that reconstruction of past dripwater Na concentrations and wind intensity will depend on accurate inference of the non-constant Na incorporation into speleothem calcite, including accounting for the role of FI and the apparent effect of organic colloids and/or coupled substitution on incorporation rates. To avoid any incorporation processes, direct measurement of FI's (for trace elements) could reproduce paleo-dripwater chemistry. However, this would be a new method needing careful evaluation.

### 4.5 Controls on spatial variations in trace element incorporation

#### 4.5.1 Relationship of defects with partitioning in different growth layers

It has been proposed that Sr partitioning is favored in compact calcite because of the sterically unhindered space provided by the spiral growth mechanism, whereas Mg favors porous microcrystalline fabric (Chiarini et al., 2017). We observe contrasting associations between Sr and compact vs defect-rich growth layers, which suggests that controls on Sr incorporation may be more complex. In SS1, we observe that the growth layers with highest Sr are those with low density of defects and visible FI's, although FTIR suggest that these high Sr calcite layers feature more submicroscopic fluid inclusions (Fig. 12). In MR1, we observe minimal Sr in growth layers featuring larger FI's and greater water content (Fig. 13), however in this sample the high water content layers are not the most compact calcite. These observations suggest that the submicroscopic textures regulating FI density may be the most significant scale in which Sr incorporation and water incorporation is coupled during deposition of growth layers under varying conditions.

#### 4.5.2 The origin of crosscutting features

While the variation of trace elements, organics, and defects among growth layers can be readily attributed to changing dripwater or cave conditions over time, lateral variations along growth layers require novel explanations. In many of our active samples, we observe variations in water content and trace elements, and sometimes fluorescence, which crosscut growth layers. In thin section images, similar crosscutting zones of disrupted layers have been reported elsewhere (e.g. Fig. 1 in

In review

642 Martín-Chivelet et al., 2013, Fig. 2c in Treble et al., 2017). In our actively growing stalagmites, these
643 features are not related to individual crystallites since the polarized images reveal big single crystals
644 and disturbance within the area of homogeneous extinction. Nevertheless, it is possible that elongated
645 crystallites reveal disturbed zones or crystal splitting due to strain built up between competing
646 minerals of same optical properties. This might be revealed in the often observed radial structure of a
647 polished stalagmite slab showing individual crystals (so called Spherocrystals) due to chemical
648 splitting (Self and Hill, 2003). This phenomenon may also occur on the submillimeter scale as
649 observed in our samples. Alternatively, we cannot rule out that multiple crystals grew separately but
650 at the same orientation and left residual intra-crystallite variation and suturing, but no change in
651 extinction angles.

652 These narrow crosscutting zones could also arise as contraction features if $CaCO_3$ deposition
653 proceeded by precursor phases with a higher unit cell volume such as monohydrocalcite (MHC) or
654 amorphous calcium carbonate (ACC), so that transformation to calcite such zones leave space behind
655 which can be filled by secondary precipitation. The secondary infill may have a different chemical
656 composition. Since ACC traps more trace elements (Blue et al., 2017, Littlewood et al., 2017), the
657 calcite sectors inherited from the precursor phases would be expected to retain higher trace element
658 concentrations, compared to zones of secondary infill precipitated directly by ion by ion growth of
659 calcite. Secondary infillings might form at slower rates due to slower degassing in thicker water
660 films, since these vertical disturbed zones are often marked by a concavity in the growth layer. The
661 potential for secondary precipitation and void closure is consistent with other studies analyzing fluid
662 inclusion noble gas content which led to the suggestion of a long closure process for some pores by
663 secondary carbonate infilling (Ghadiri et al., 2018).

664 Where such crosscutting features are prevalent in speleothems, they may be intersected by LA-ICP-
665 MS line tracks, introducing pronounced transient anomalies in elements such as Sr which could be
666 misinterpreted as growth layers of anomalously low Sr. Careful examination of calcite fabric by
667 either transmitted light or CLSM might prove useful to avoid such zones when configuring laser
668 ablation tracks. As this study highlights, LA maps combined with other non-destructive mapping
669 techniques such as TL images, FTIR or CLSM yield the most detailed information about trace
670 element distribution and allows to interpret trace element variations in relation to crystal features,
671 organics, fluid inclusions and other phases.

672 **5 Conclusions**

673 We combined non-destructive mapping techniques with LA-ICP-MS trace element mapping in a
674 high-resolution study examining one to two decades of growth in three active stalagmites, and
675 centuries of growth in a fossil stalagmite. Using FTIR to map the distribution of water in calcite, we
676 find that water is not only hosted in microscopic FI's visible in transmitted light microscopy, but can
677 also be hosted in compact calcite without visual defects as submicroscopic FI's. Our results suggest
678 that these FI's can host a significant fraction of highly incompatible elements such as Na, in
679 stalagmites with low Na incorporation in the calcite phase. Our results also suggest that coupled
680 substitution of $Y^{3+}$ and $Na^{+}$ increases solid phase Na incorporation in stalagmites with high Y
681 delivery. It remains to be explored whether fluid inclusions also host significant fraction of Li, a
682 monovalent ion with effective partitioning coefficients in calcite 10-fold higher than Na (Füger et al.,
683 2019) but still 100-fold lower than Mg (Wassenburg et al., 2020). If fluid Li were significant and
684 variable, it would need to be considered in the interpretation of Li isotopic records of speleothems.

In review



This is a provisional file, not the final typeset article

In active stalagmites, we observe that fluorescent organic matter is generally co-located with areas of high 2983 $cm^{-1}$ band linear absorbance, highlighting the potential of FTIR as an additional technique to map the distribution of organics in stalagmites. In one sample (MR1), 2983 $cm^{-1}$ band absorbance distinguishes organic rich growth layers not resolved in fluorescence. Among the different active stalagmites, the sample with greatest fluorescence also corresponds to highest Y, but within a given sample, growth layers with highest concentrations of colloidally transported elements do not universally coincide with peak fluorescence or FTIR 2983 $cm^{-1}$ band absorbance. We also find that layers with higher concentrations of organic matter do not feature a higher density of defects or fluid inclusions.

In several active stalagmites, apparently within a single crystallite, growth layers are interrupted by narrow crosscutting zones of lower fluorescence and Sr content. Several crystallization processes may contribute to these disturbed zones. When such zones are intersected by LA-ICP-MS single line transects across the stalagmite, they may be misinterpreted as anomalously low Sr growth layers. This study demonstrates the importance of assessing controlling mechanisms of trace element distribution and incorporation into stalagmite samples to better constrain the relationship between speleothem trace elements and paleoenvironmental interpretations.

## 6 Figure captions

**Figure 1.** Representative FTIR spectrum (800-4000 $cm^{-1}$) from sample SS2 indicating the 3400 $cm^{-1}$ bands (water) and 2983 $cm^{-1}$ bands (organics) which are processed in this study.

**Figure 2.** Images and maps of GLA. a) TL image with sequential focal plane and crossed polars b) CLSM image, c) normalized intensity map of the linear absorbance of the 3400 $cm^{-1}$ band, d) linear absorbance of the 2983 $cm^{-1}$ band.

**Figure 3.** Images and maps of SS2. a) TL image with sequential focal plane b) CLSM image, c) normalized intensity map of the linear absorbance of the 3400 $cm^{-1}$ band, d) linear absorbance of the 2983 $cm^{-1}$ band.

**Figure 4.** Images and maps of SS1. a) TL image with sequential focal plane b) CLSM image, c) normalized intensity map of the linear absorbance of the 3400 $cm^{-1}$ band, d) linear absorbance of the 2983 $cm^{-1}$ band.

**Figure 5.** Images and maps of MR1. a) TL image with sequential focal plane b) CLSM image, c) normalized intensity map of the linear absorbance of the 3400 $cm^{-1}$ band, d) linear absorbance of the 2983 $cm^{-1}$ band.

**Figure 6.** Images and maps of PG2. a) TL image with sequential focal plane b) CLSM image, c) normalized intensity map of the linear absorbance of the 3400 $cm^{-1}$ band, d) linear absorbance of the 2983 $cm^{-1}$ band.

**Figure 7.** For all samples, FTIR map comparison showing linear absorbance at 3400 $cm^{-1}$, normalized linear absorbance of the 3400 $cm^{-1}$ band, ratio of linear absorbances of the 3400 $cm^{-1}$ and 2983 $cm^{-1}$ bands, and linear absorbance at 2983 $cm^{--1}$.

In review

**Figure 8.** Histograms of elements Mg, Si, Na, U, and Y in all samples based on LA-ICP-MS mapped area for all mapped pixels in which the Al content was <6 ppm (and Ca counts were > 800'000 CPS), in order to evaluate the concentrations in calcite with limited effect from embedded detrital phases. The green line illustrates the median concentration.

**Figure 9.** Incorporation coefficients of elements based on the median concentration illustrated in Figure 8, and the mean and range of dripwater chemistry for that location, from Sliwinski et al. (2023). Estimation assumes modern dripwater is representative of that during the integrated period of stalagmite growth, and assumes that stalagmites maintain a high f so that dripwater does not evolve significantly during the deposition interval.

**Figure 10.** Images and maps of GLA. a) cross polarized TL image, b) CLSM image, c) normalized linear absorbance of the 3400 $cm^{-1}$ band indicating water distribution, d-i) LA-ICP-MS element maps of different elements (concentrations in ppm) as labeled in each image.

**Figure 11.** Images and maps of SS2. a) cross polarized TL image, b) CLSM image, c) normalized linear absorbance of the 3400 $cm^{-1}$ band indicating water distribution, d-i) LA-ICP-MS element maps of different elements (concentrations in ppm) as labeled in each image.

**Figure 12.** Images and maps of SS1. a) TL image, b) CLSM image, c) normalized linear absorbance of the 3400 $cm^{-1}$ band indicating water distribution, d-i) LA-ICP-MS element maps of different elements (concentrations in ppm) as labeled in each image.

**Figure 13.** Images and maps of MR1. a) cross polarized TL image, b) normalized linear absorbance of the 2983 $cm^{-1}$ band, c) normalized linear absorbance of the 3400 $cm^{-1}$ band indicating water distribution, d-i) LA-ICP-MS element maps of different elements (concentrations in ppm) as labeled in each image.

**Figure 14.** Images and maps of PG2. a) cross polarized TL image, b) CLSM image, c) normalized linear absorbance of the 3400 $cm^{-1}$ band indicating water distribution, d-i) LA-ICP-MS element maps of different elements (concentrations in ppm) as labeled in each image.

## 7 Tables

Table 1: Sample information based on monitoring data by Sliwinski et al. (2023) and Kost et al. (2022).

| Sample | average growth rate [µm/yr] | Growth season | Mean drip rate [mL/min] | Mean Mg/Ca dripwater [mmol/mol] |
|---|---|---|---|---|
| PG | 66 | winter* | 0.37 | 477 |
| SS | 130 | summer/winter | 92 | 37 |
| MR | 150 | unknown | 3 | 53 |
| GLA | 3 | unknown | - | - |

In review



This is a provisional file, not the final typeset article

754 *not every winter season according to the monitoring study of Kost et al. (2022)

755 **8 References**


756 AFFOLTER, S., FLEITMANN, D. & LEUENBERGER, M. 2014. New online method for water
757 isotope analysis of speleothem fluid inclusions using laser absorption spectroscopy (WS-
758 CRDS). *Clim. Past,* 10**,** 1291-1304.

759 ARTZ, R. R. E., CHAPMAN, S. J., JEAN ROBERTSON, A. H., POTTS, J. M., LAGGOUN-
760 DÉFARGE, F., GOGO, S., COMONT, L., DISNAR, J.-R. & FRANCEZ, A.-J. 2008. FTIR
761 spectroscopy can be used as a screening tool for organic matter quality in regenerating
762 cutover peatlands. *Soil Biology and Biochemistry,* 40**,** 515-527.

763 BLUE, C. R., GIUFFRE, A., MERGELSBERG, S., HAN, N., DE YOREO, J. J. & DOVE, P. M.
764 2017. Chemical and physical controls on the transformation of amorphous calcium carbonate
765 into crystalline CaCO3 polymorphs. *Geochimica et Cosmochimica Acta,* 196**,** 179-196.

766 BORSATO, A., FAIRCHILD, I. J., FRISIA, S., WYNN, P. M. & FOHLMEISTER, J. 2023. The
767 Ernesto Cave, northern Italy, as a candidate auxiliary reference section for the definition of
768 the Anthropocene series. *The Anthropocene Review,* 0.

769 BORSATO, A., FRISIA, S., FAIRCHILD, I. J., SOMOGYI, A. & SUSINI, J. 2007. Trace element
770 distribution in annual stalagmite laminae mapped by micrometer-resolution X-ray
771 fluorescence: Implications for incorporation of environmentally significant species.
772 *Geochimica et Cosmochimica Acta,* 71**,** 1494-1512.

773 BUSENBERG, E. & PLUMMER, N. L. 1985. Kinetic and thermodynamic factors controlling the
774 distribution of SO32− and Na+ in calcites and selected aragonites. *Geochimica et*
775 *Cosmochimica Acta,* 49**,** 713-725.

776 CHALMIN, E., PERRETTE, Y., FANGET, B. & SUSINI, J. 2013. Investigation of Organic Matter
777 Entrapped in Synthetic Carbonates—A Multimethod Approach. *Microscopy and*
778 *Microanalysis,* 19**,** 132-144.

779 CHIARINI, V., COUCHOUD, I., DRYSDALE, R., BAJO, P., MILANOLO, S., FRISIA, S., GREIG,
780 A., HELLSTROM, J. & DE WAELE, J. 2017. Petrographical and geochemical changes in
781 Bosnian stalagmites and their palaeo-environmental significance. *International Journal of*
782 *Speleology,* 46**,** 33-49.

783 CURTI, E. 1997. Coprecipitation of radionuclides: basic concepts, literature review and first
784 applications. Würenlingen: Paul Scherrer Institute (PSI).

785 DAY, C. C. & HENDERSON, G. M. 2013. Controls on trace-element partitioning in cave-analogue
786 calcite. *Geochimica et Cosmochimica Acta,* 120**,** 612-627.

787 DE YOREO, J. J. & VEKILOV, P. G. 2003. Principles of Crystal Nucleation and Growth. *Reviews in*
788 *Mineralogy and Geochemistry,* 54**,** 57-93.

789 DEMÉNY, A., NÉMETH, P., CZUPPON, G., LEÉL-ŐSSY, S., SZABÓ, M., JUDIK, K., NÉMETH,
790 T. & STIEBER, J. 2016. Formation of amorphous calcium carbonate in caves and its
791 implications for speleothem research. *Scientific Reports,* 6**,** 39602.

792 DEVRIENDT, L. S., MEZGER, E. M., OLSEN, E. K., WATKINS, J. M., KACZMAREK, K.,
793 NEHRKE, G., DE NOOIJER, L. J. & REICHART, G. J. 2021. Sodium incorporation into
794 inorganic CaCO3 and implications for biogenic carbonates. *Geochimica et Cosmochimica*
795 *Acta,* 314**,** 294-312.


In review

ENGIN, B., DEMIRTAŞ, H. & EKEN, M. 2006. Temperature effects on egg shells investigated by XRD, IR and ESR techniques. *Radiation Physics and Chemistry,* 75**,** 268-277.

FRISIA, S. 2015. Microstratigraphic logging of calcite fabrics in speleothems as tool for palaeoclimate studies. *International Journal of Speleology,* 44**,** 1-16.

FRISIA, S., BORSATO, A. & HELLSTROM, J. 2018. High spatial resolution investigation of nucleation, growth and early diagenesis in speleothems as exemplar for sedimentary carbonates. *Earth-Science Reviews,* 178**,** 68-91.

FÜGER, A., KONRAD, F., LEIS, A., DIETZEL, M. & MAVROMATIS, V. 2019. Effect of growth rate and pH on lithium incorporation in calcite. *Geochimica et Cosmochimica Acta,* 248**,** 14-24.

GÁZQUEZ, F., CALAFORRA, J.-M., RULL, F., FORTI, P. & GARCÍA-CASCO, A. 2012. Organic matter of fossil origin in the amberine speleothems from El Soplao Cave (Cantabria, Northern Spain).

GHADIRI, E., VOGEL, N., BRENNWALD, M. S., MADEN, C., HÄUSELMANN, A. D., FLEITMANN, D., CHENG, H. & KIPFER, R. 2018. Noble gas based temperature reconstruction on a Swiss stalagmite from the last glacial–interglacial transition and its comparison with other climate records. *Earth and Planetary Science Letters,* 495**,** 192-201.

GREEN, D. C., IHLI, J., THORNTON, P. D., HOLDEN, M. A., MARZEC, B., KIM, Y.-Y., KULAK, A. N., LEVENSTEIN, M. A., TANG, C., LYNCH, C., WEBB, S. E. D., TYNAN, C. J. & MELDRUM, F. C. 2016. 3D visualization of additive occlusion and tunable full-spectrum fluorescence in calcite. *Nature Communications,* 7**,** 13524.

HARTLAND, A., FAIRCHILD, I. J., LEAD, J. R., BORSATO, A., BAKER, A., FRISIA, S. & BAALOUSHA, M. 2012. From soil to cave: Transport of trace metals by natural organic matter in karst dripwaters. *Chemical Geology,* 304-305**,** 68-82.

HARTLAND, A., FAIRCHILD, I. J., MÜLLER, W. & DOMINGUEZ-VILLAR, D. 2014. Preservation of NOM-metal complexes in a modern hyperalkaline stalagmite: Implications for speleothem trace element geochemistry. *Geochimica et Cosmochimica Acta,* 128**,** 29-43.

ISHIKAWA, M. & ICHIKUNI, M. 1984. Uptake of sodium and potassium by calcite. *Chemical Geology,* 42**,** 137-146.

KOST, O., GONZÁLEZ-LEMOS, S., RODRIGUEZ-RODRIGUEZ, L., SLIWINSKI, J., ENDRES, L., HAGHIPOUR, N. & STOLL, H. 2022. Relationship of seasonal variations in drip water δ13CDIC, δ18O and trace elements with surface and physical cave conditions of La Vallina Cave, NW Spain. *Hydrol. Earth Syst. Sci. Discuss.,* 2022**,** 1-42.

KOST, O. & STOLL, H. 2023. Marine aerosols in coastal areas and their impact on cave drip water – A monitoring study from Northern Spain. *Atmospheric Environment,* 302**,** 119730.

KRÜGER, Y., MARTI, D., STAUB, R. H., FLEITMANN, D. & FRENZ, M. 2011. Liquid–vapour homogenisation of fluid inclusions in stalagmites: Evaluation of a new thermometer for palaeoclimate research. *Chemical Geology,* 289**,** 39-47.

LEBRON, I. & SUAREZ, D. L. 1996. Calcite nucleation and precipitation kinetics as affected by dissolved organic matter at 25°C and pH > 7.5. *Geochimica et Cosmochimica Acta,* 60**,** 2765-2776.

In review



This is a provisional file, not the final typeset article

LINDEMAN, I., HANSEN, M., SCHOLZ, D., BREITENBACH, S. F. M. & HARTLAND, A. 2022. Effects of organic matter complexation on partitioning of transition metals into calcite: Cave-analogue crystal growth experiments. *Geochimica et Cosmochimica Acta,* 317**,** 118-137.

LITTLEWOOD, J. L., SHAW, S., PEACOCK, C. L., BOTS, P., TRIVEDI, D. & BURKE, I. T. 2017. Mechanism of Enhanced Strontium Uptake into Calcite via an Amorphous Calcium Carbonate Crystallization Pathway. *Crystal Growth & Design,* 17**,** 1214-1223.

MARTÍN-CHIVELET, J., MUÑOZ-GARCÍA, M. B., ORTEGA, A. I., CRUZ-MARTÍNEZ, J., GARRALÓN, A. & TURRERO, M. J. Speleothem microstratigraphy: some clues for paleoclimate series reconstruction at centennial to decadal scales. 2013.

MARTÍNEZ-PILLADO, V., YUSTA, I., IRIARTE, E., ÁLVARO, A., ORTEGA, N., ARANBURU, A. & ARSUAGA, J. L. 2020. The red coloration of Goikoetxe Cave's speleothems (Busturia, Spain): An indicator of paleoclimatic changes. *Quaternary International,* 566-567**,** 141-151.

MECKLER, A. N., AFFOLTER, S., DUBLYANSKY, Y. V., KRÜGER, Y., VOGEL, N., BERNASCONI, S. M., FRENZ, M., KIPFER, R., LEUENBERGER, M., SPÖTL, C., CAROLIN, S., COBB, K. M., MOERMAN, J., ADKINS, J. F. & FLEITMANN, D. 2015. Glacial–interglacial temperature change in the tropical West Pacific: A comparison of stalagmite-based paleo-thermometers. *Quaternary Science Reviews,* 127**,** 90-116.

MELDRUM, F. C. & HYDE, S. T. 2001. Morphological influence of magnesium and organic additives on the precipitation of calcite. *Journal of Crystal Growth,* 231**,** 544-558.

PAQUETTE, J. & REEDER, R. J. 1995. Relationship between surface structure, growth mechanism, and trace element incorporation in calcite. *Geochimica et Cosmochimica Acta,* 59**,** 735-749.

PATERSON, M. 1982. The determination of hydroxyl by infrared absorption in quartz, silicate glasses and similar materials. *Bulletin de minéralogie,* 105**,** 20-29.

PATON, C., HELLSTROM, J., PAUL, B., WOODHEAD, J. & HERGT, J. 2011. Iolite: Freeware for the visualisation and processing of mass spectrometric data. *Journal of Analytical Atomic Spectrometry,* 26**,** 2508-2518.

PEARSON, A. R., HARTLAND, A., FRISIA, S. & FOX, B. R. 2020a. Formation of calcite in the presence of dissolved organic matter: Partitioning, fabrics and fluorescence. *Chemical Geology,* 539**,** 119492.

PEARSON, A. R., HARTLAND, A., FRISIA, S. & FOX, B. R. S. 2020b. Formation of calcite in the presence of dissolved organic matter: Partitioning, fabrics and fluorescence. *Chemical Geology,* 539**,** 119492.

PHILLIPS, B. L., ZHANG, Z., KUBISTA, L., FRISIA, S. & BORSATO, A. 2016. NMR spectroscopic study of organic phosphate esters coprecipitated with calcite. *Geochimica et Cosmochimica Acta,* 183**,** 46-62.

RENARD, F., MONTES-HERNANDEZ, G., RUIZ-AGUDO, E. & PUTNIS, C. V. 2013. Selenium incorporation into calcite and its effect on crystal growth: An atomic force microscopy study. *Chemical Geology,* 340**,** 151-161.

RIMSTIDT, J. D., BALOG, A. & WEBB, J. 1998. Distribution of trace elements between carbonate minerals and aqueous solutions. *Geochimica et Cosmochimica Acta,* 62**,** 1851-1863.

RUTLIDGE, H., BAKER, A., MARJO, C. E., ANDERSEN, M. S., GRAHAM, P. W., CUTHBERT, M. O., RAU, G. C., ROSHAN, H., MARKOWSKA, M., MARIETHOZ, G. & JEX, C. N. 2014. Dripwater organic matter and trace element geochemistry in a semi-arid karst

In review

environment: Implications for speleothem paleoclimatology. *Geochimica et Cosmochimica Acta,* 135**,** 217-230.

SELF, C. A. & HILL, C. A. 2003. How speleothems grow: an introduction to the ontogeny of cave minerals. *Journal of Cave and Karst Studies,* 65**,** 130-151.

SLIWINSKI, J. T., KOST, O., ENDRES, L., IGLESIAS, M., HAGHIPOUR, N., GONZÁLEZ-LEMOS, S. & STOLL, H. M. 2023. Exploring soluble and colloidally transported trace elements in stalagmites: The strontium-yttrium connection. *Geochimica et Cosmochimica Acta,* 343**,** 64-83.

SLIWINSKI, J. T. & STOLL, H. M. 2021. Combined fluorescence imaging and LA-ICP-MS trace element mapping of stalagmites: Microfabric identification and interpretation. *Chemical Geology,* 581**,** 120397.

STÜNITZ, H., THUST, A., HEILBRONNER, R., BEHRENS, H., KILIAN, R., TARANTOLA, A. & FITZ GERALD, J. 2017. Water redistribution in experimentally deformed natural milky quartz single crystals—Implications for H2O-weakening processes. *Journal of Geophysical Research: Solid Earth,* 122**,** 866-894.

TADROS, C. V., TREBLE, P. C., BAKER, A., HANKIN, S. & ROACH, R. 2019. Cave drip water solutes in south-eastern Australia: Constraining sources, sinks and processes. *Science of The Total Environment,* 651**,** 2175-2186.

TREBLE, P. C., BAKER, A., AYLIFFE, L. K., COHEN, T. J., HELLSTROM, J. C., GAGAN, M. K., FRISIA, S., DRYSDALE, R. N., GRIFFITHS, A. D. & BORSATO, A. 2017. Hydroclimate of the Last Glacial Maximum and deglaciation in southern Australia's arid margin interpreted from speleothem records (23–15 ka). *Clim. Past,* 13**,** 667-687.

TREMAINE, D. M. & FROELICH, P. N. 2013. Speleothem trace element signatures: A hydrologic geochemical study of modern cave dripwaters and farmed calcite. *Geochimica et Cosmochimica Acta,* 121**,** 522-545.

WASSENBURG, J. A., RIECHELMANN, S., SCHRÖDER-RITZRAU, A., RIECHELMANN, D. F. C., RICHTER, D. K., IMMENHAUSER, A., TERENTE, M., CONSTANTIN, S., HACHENBERG, A., HANSEN, M. & SCHOLZ, D. 2020. Calcite Mg and Sr partition coefficients in cave environments: Implications for interpreting prior calcite precipitation in speleothems. *Geochimica et Cosmochimica Acta,* 269**,** 581-596.

WASSENBURG, J. A., VONHOF, H. B., CHENG, H., MARTÍNEZ-GARCÍA, A., EBNER, P.-R., LI, X., ZHANG, H., SHA, L., TIAN, Y., EDWARDS, R. L., FIEBIG, J. & HAUG, G. H. 2021. Penultimate deglaciation Asian monsoon response to North Atlantic circulation collapse. *Nature Geoscience,* 14**,** 937-941.

WASYLENKI, L. E., DOVE, P. M. & DE YOREO, J. J. 2005. Effects of temperature and transport conditions on calcite growth in the presence of Mg2+: Implications for paleothermometry. *Geochimica et Cosmochimica Acta,* 69**,** 4227-4236.

## 9 Conflict of Interest

*The authors declare that the research was conducted in the absence of any commercial or financial relationships that could be construed as a potential conflict of interest.*



This is a provisional file, not the final typeset article

## 10 Author Contributions

OK and HS conceived and designed the research; HS supervised the study; OK performed FTIR analyses under supervision of NG and ML, OK performed all other lab analyses; data processing was completed by OK with NG, ML, and JS; OK, JS, and HS wrote and edited the paper, all co-authors reviewed the manuscript.

## 11 Funding

This work was supported by ETH Zürich [grant number ETH-1318-1].

## 12 Acknowledgments

We thank Laura Endres for assistance processing speleothem histograms, and Stefano Bernasconi for discussion of fluid inclusions as influence on Na in stalagmites.

## 13 Supplementary Material

Supplementary material is provided in a separate file

## 1 Data Availability Statement

Data is made available on request.

In review

Figure 1.JPEG

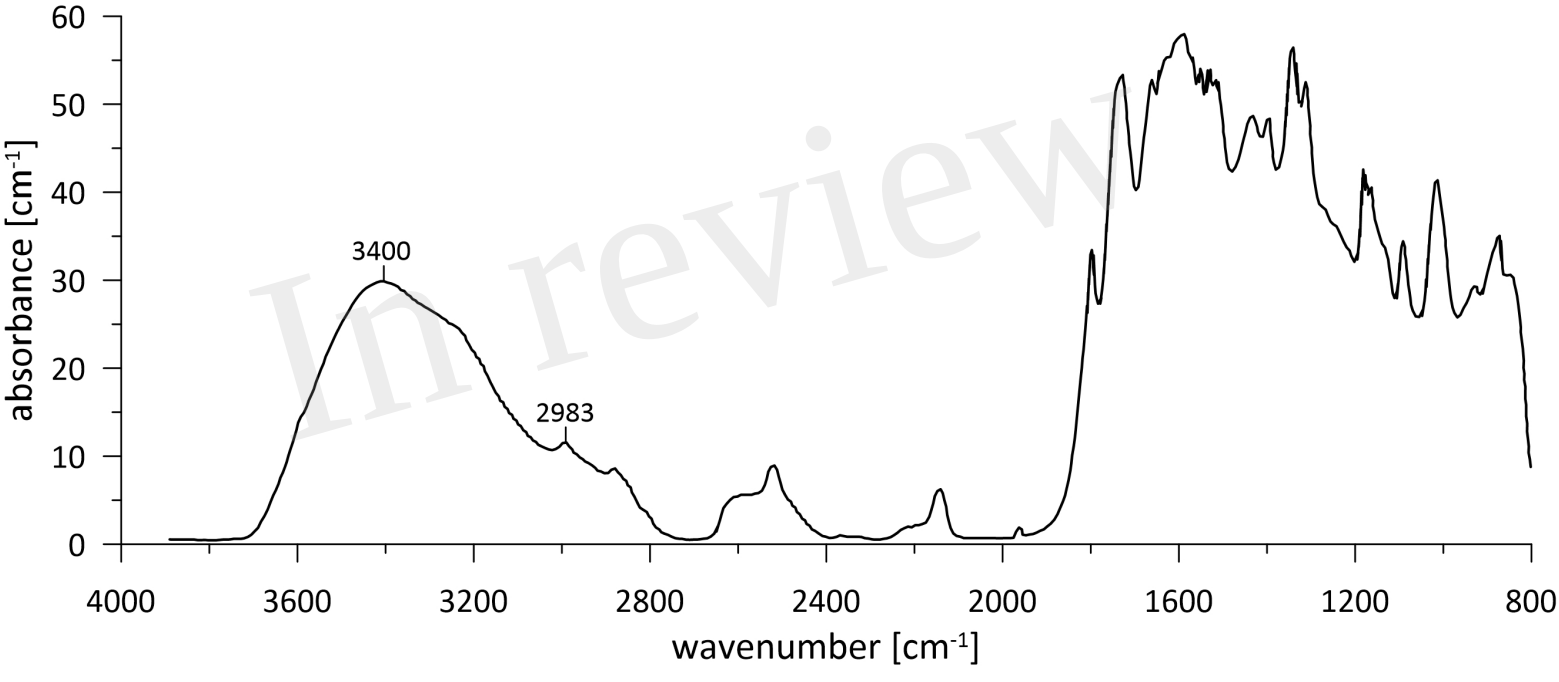


In review

Figure 2.JPEG

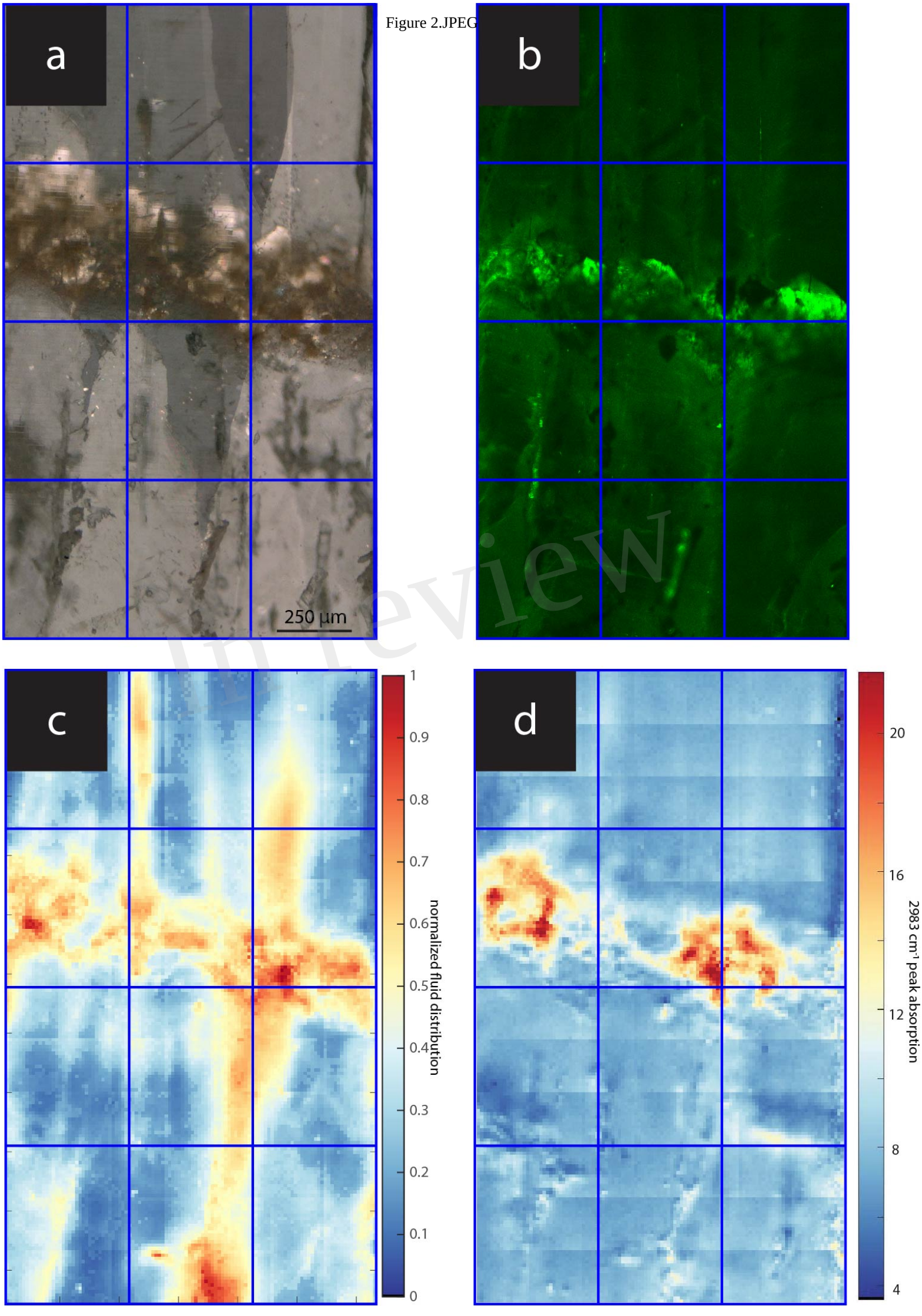


In review

Figure 3.JPEG

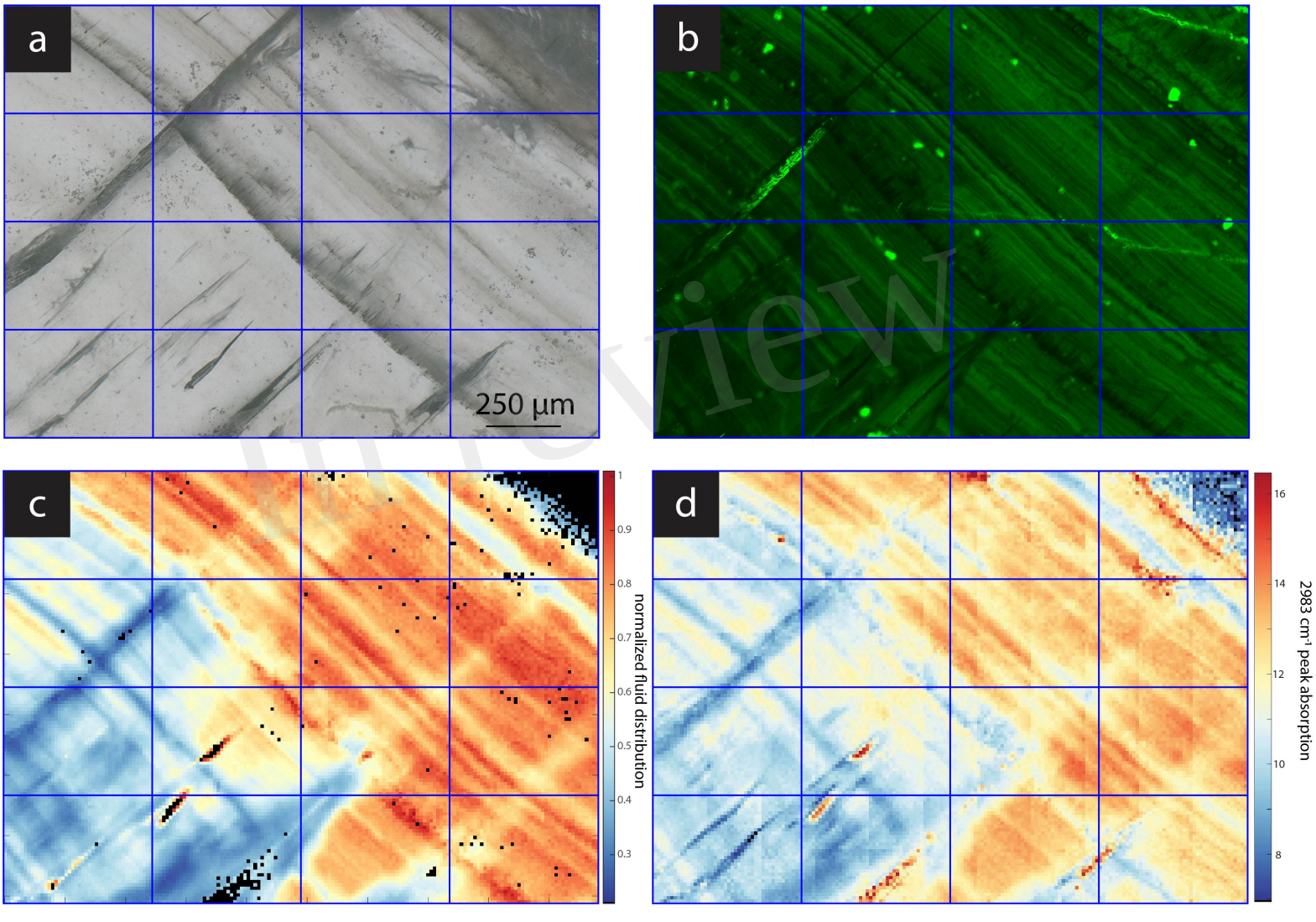


Preview

Figure 4.JPEG

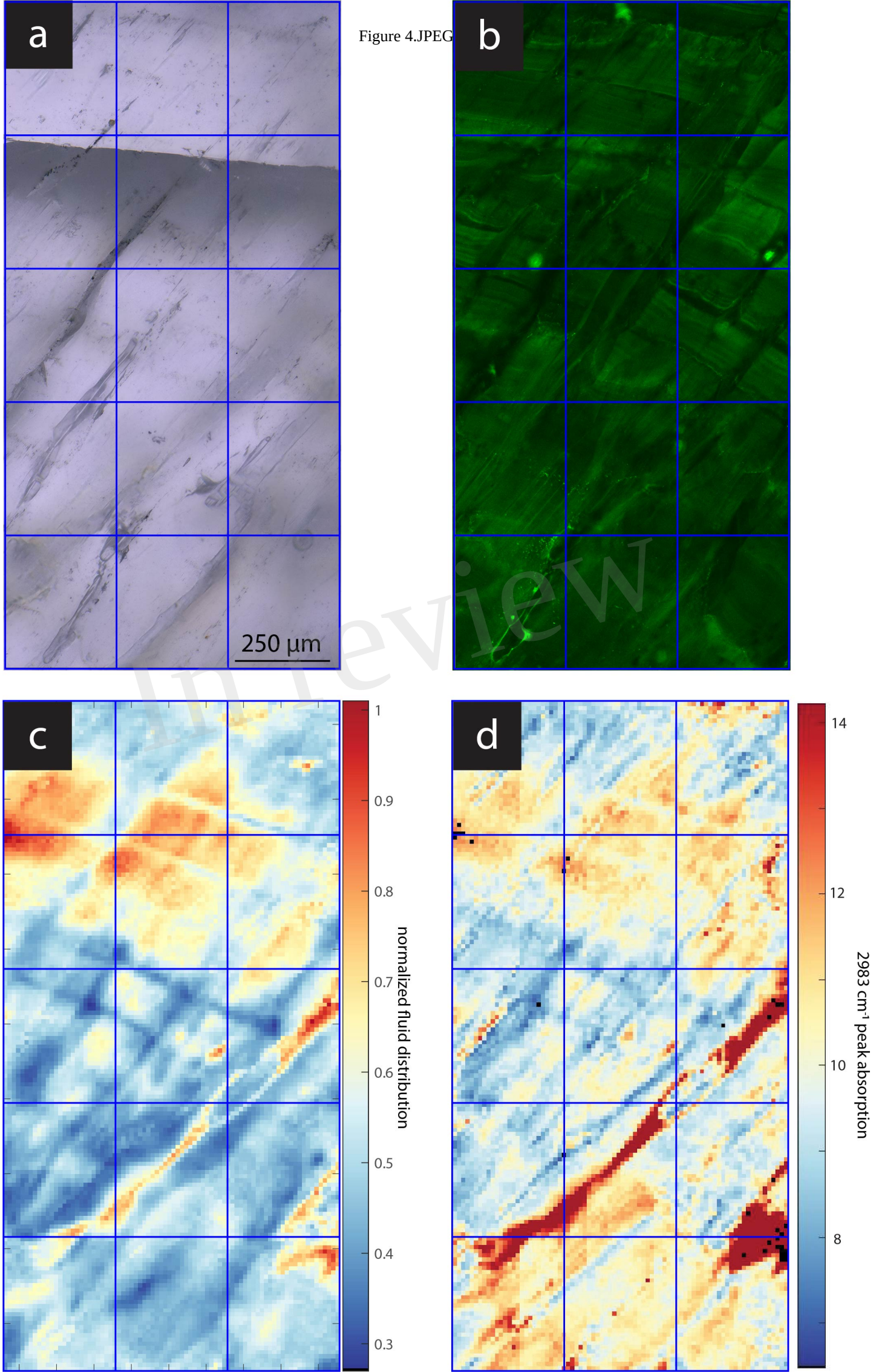


In review

Figure 5.JPE

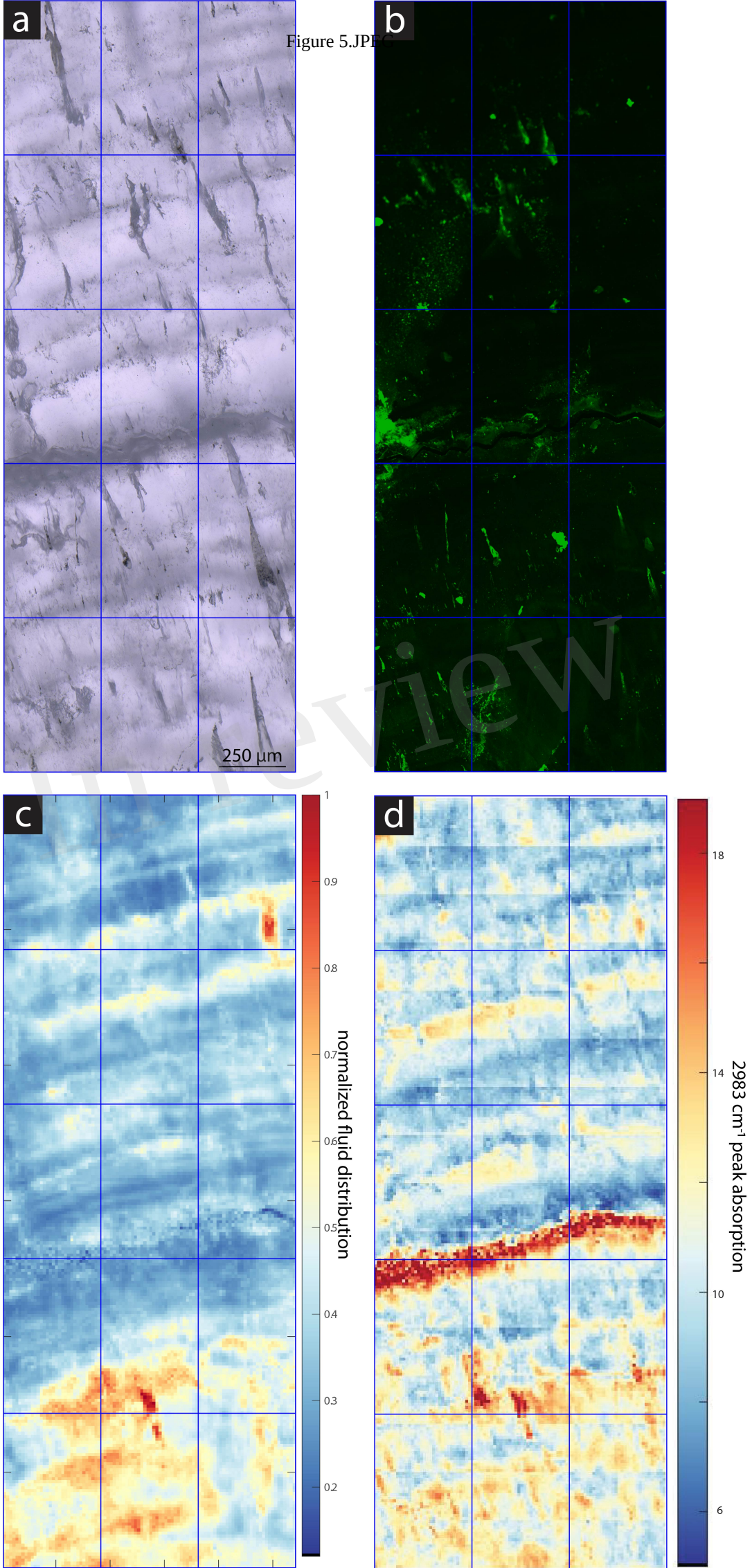


Preview

Figure 6.JPEG

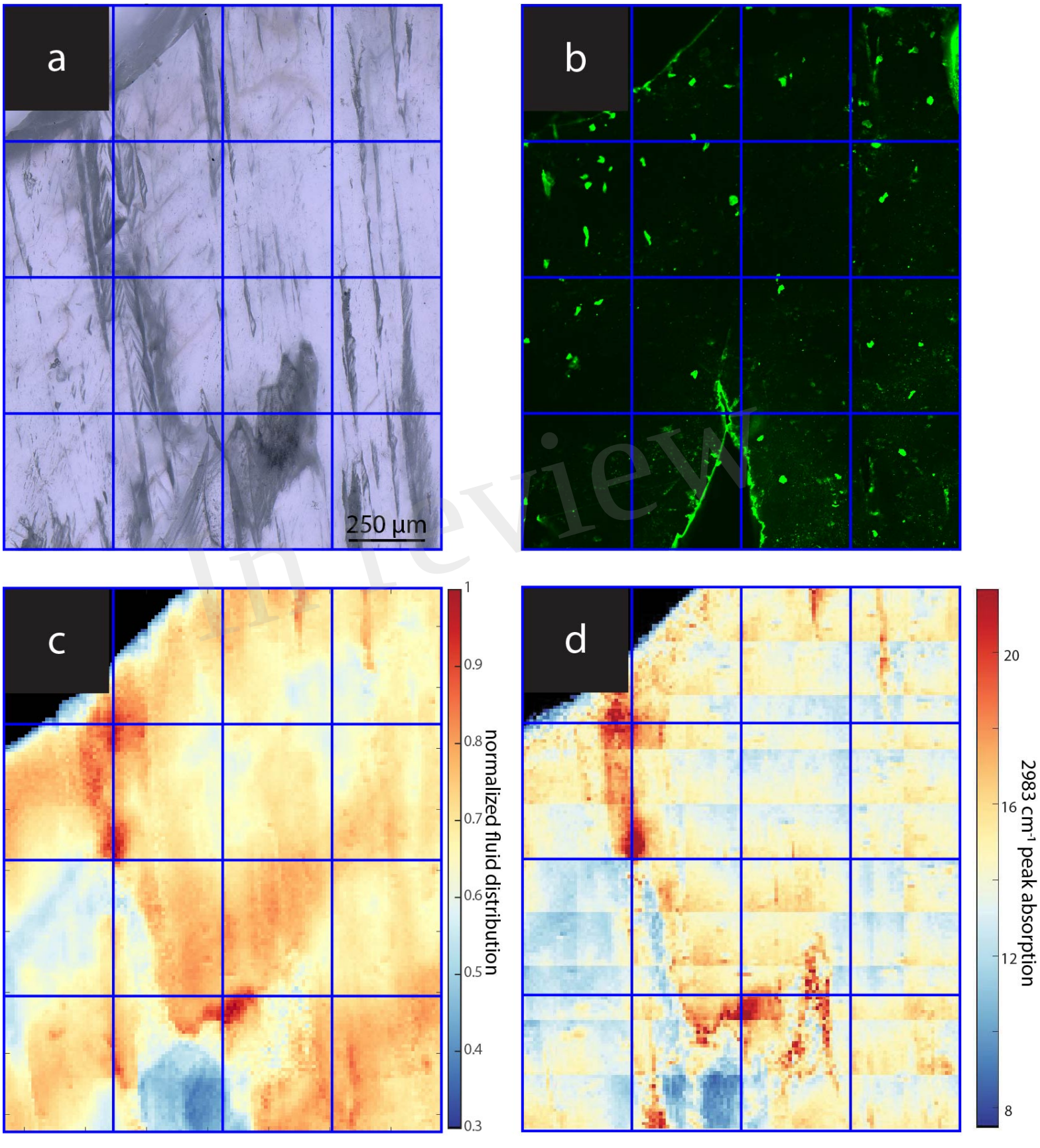


In review

Figure 7.JPEG

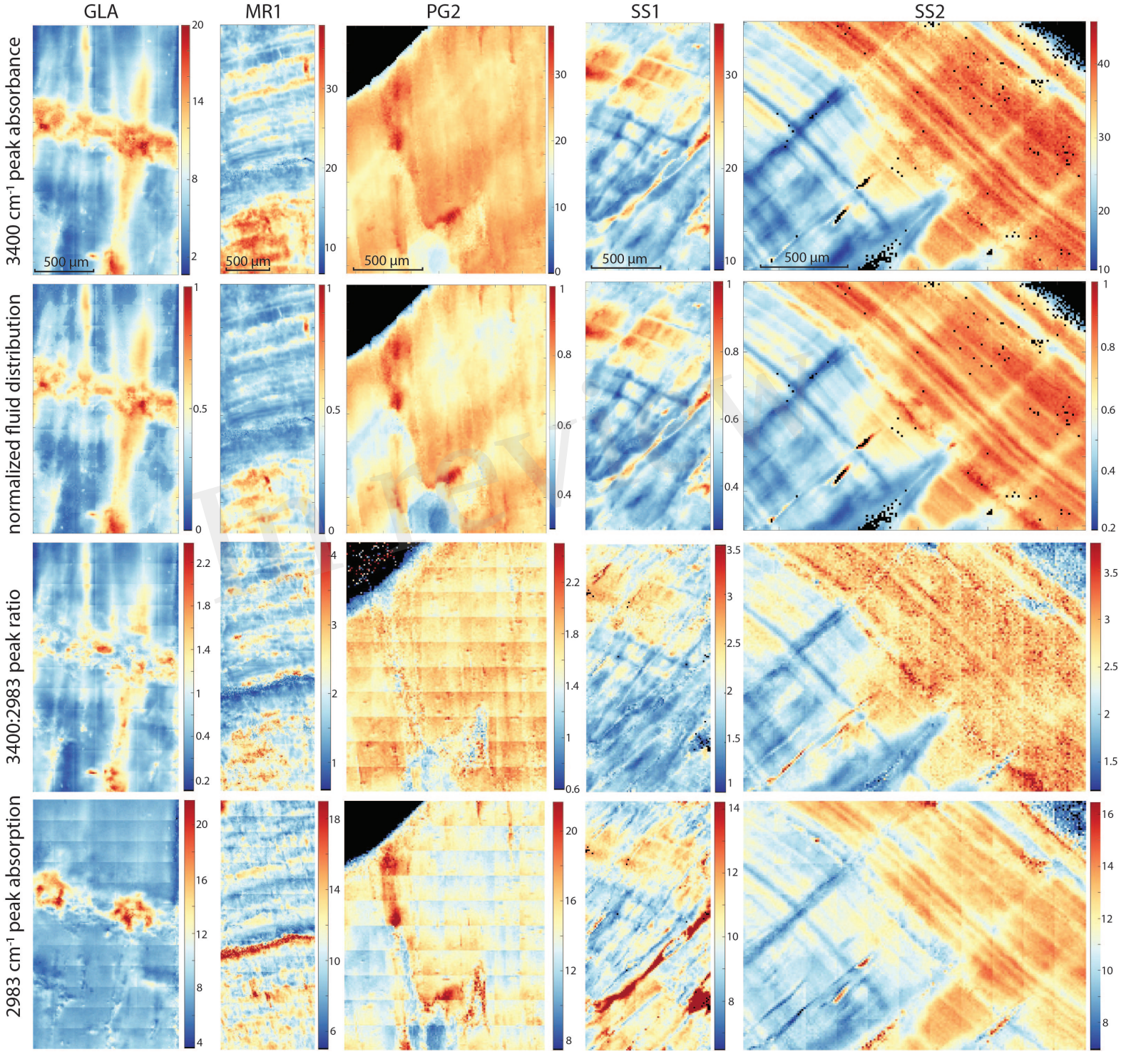

Figure 8.JPEG

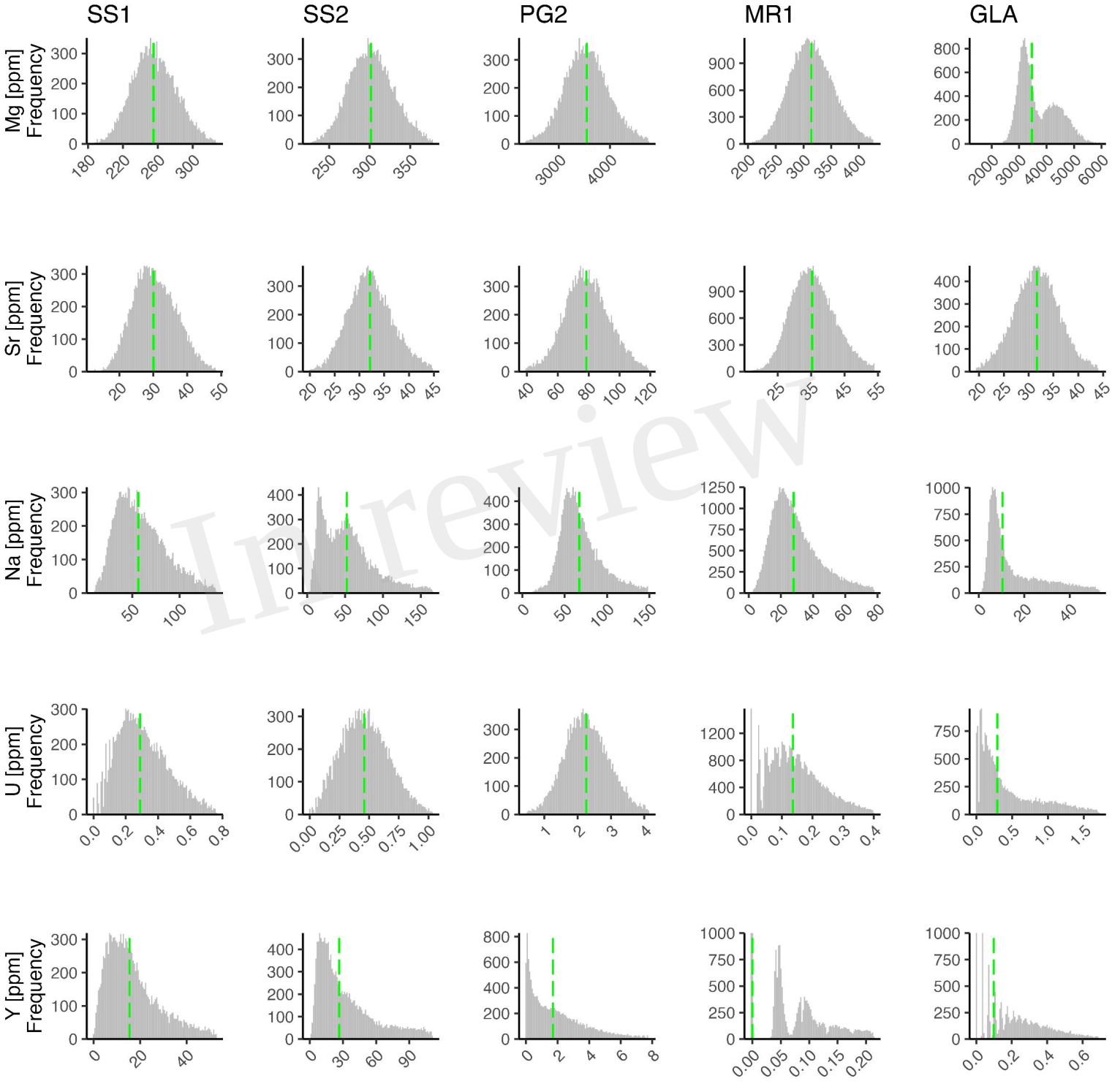


Inreview

Figure 9.JPEG

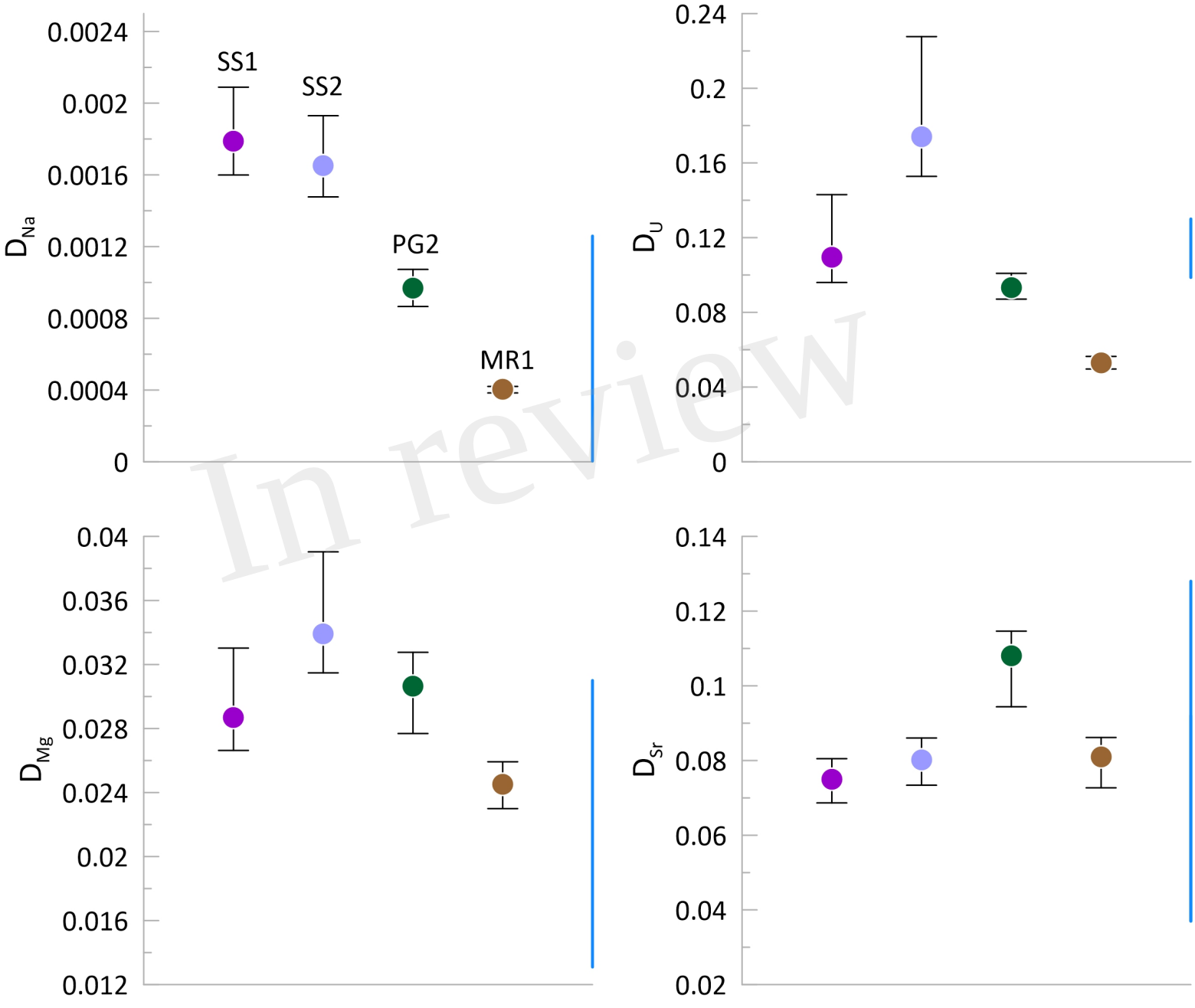


In review

Figure 10.JPEG

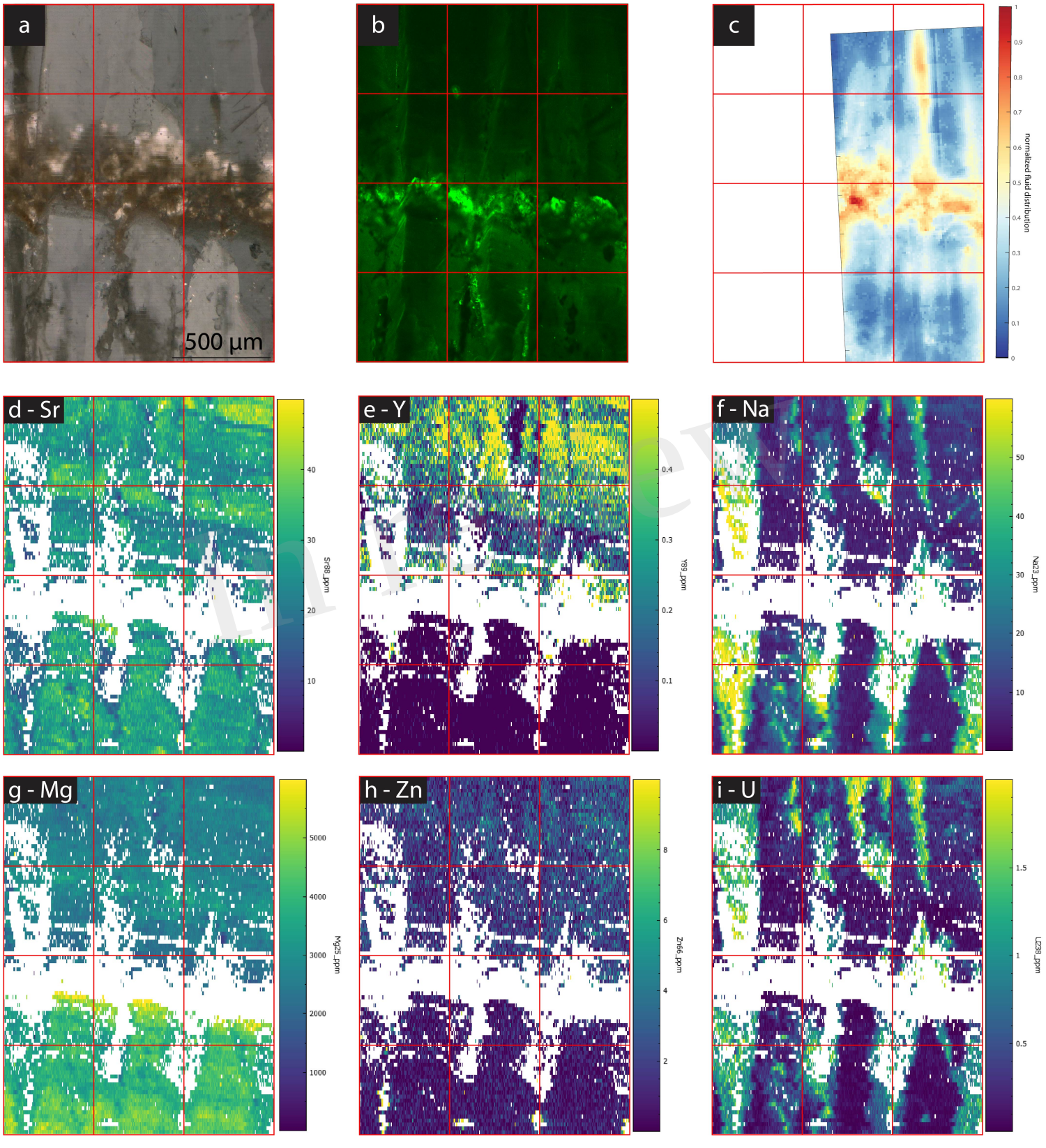

Figure 11.JPEG

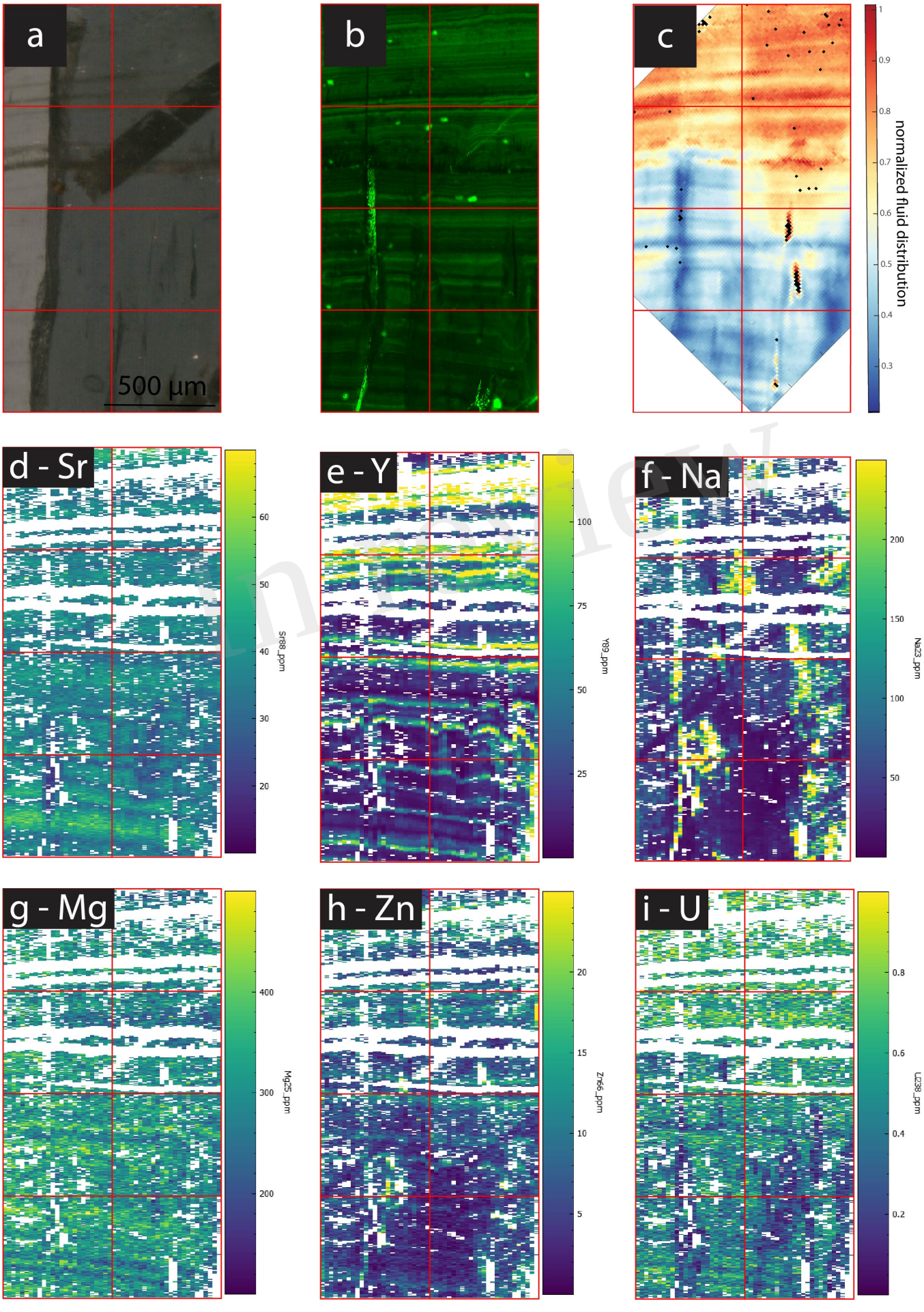

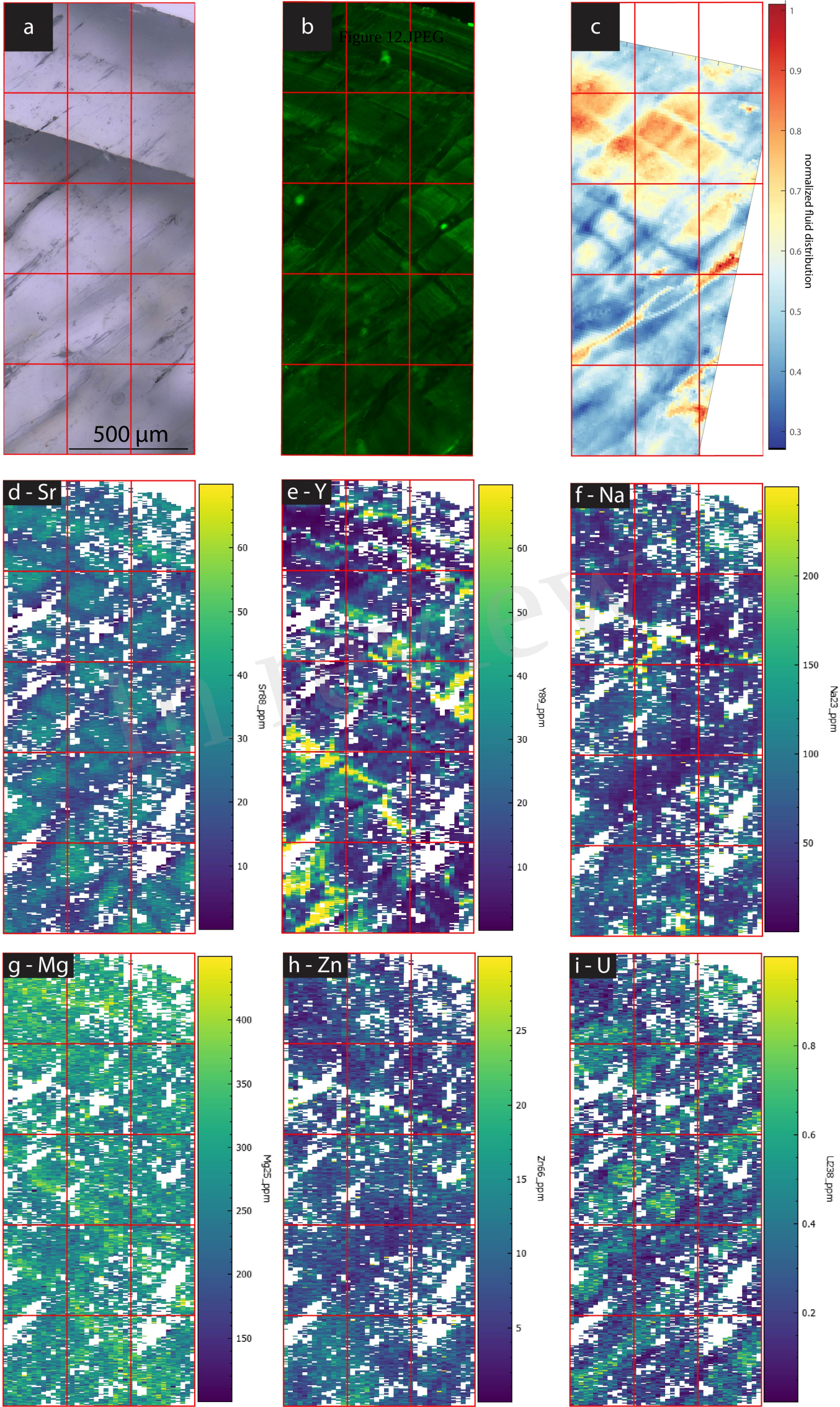
a
500 µm
b
Figure 12.JPEG
c
normalized fluid distribution
1
0.9
0.8
0.7
0.6
0.5
0.4
0.3
d - Sr
Sr88_ppm
60
50
40
30
20
10
e - Y
Y89_ppm
60
50
40
30
20
10
f - Na
Na23_ppm
200
150
100
50
g - Mg
Mg25_ppm
400
350
300
250
200
150
h - Zn
Zn66_ppm
25
20
15
10
5
i - U
U238_ppm
0.8
0.6
0.4
0.2

Figure 13.JPEG

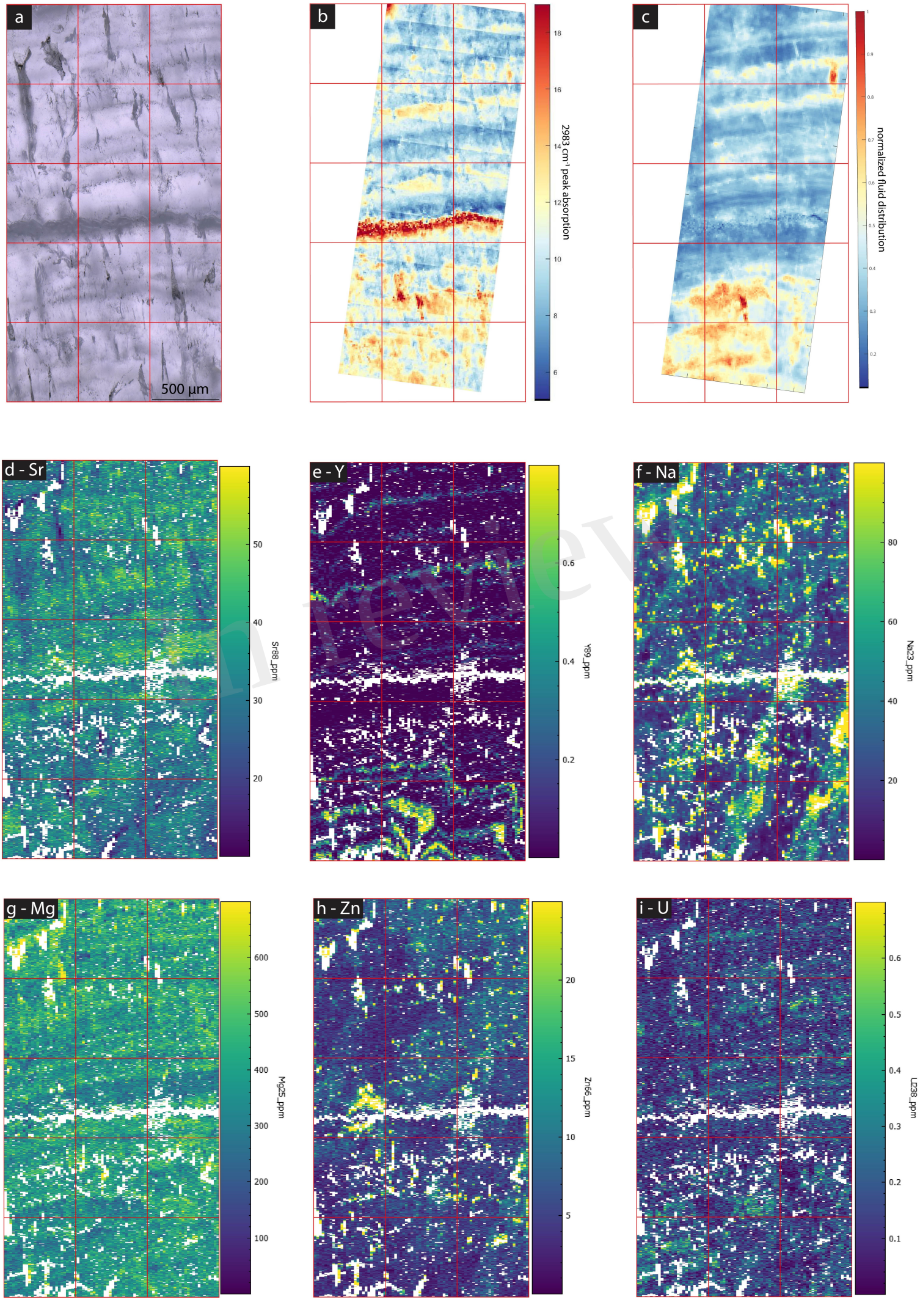

Figure 14.JPEG

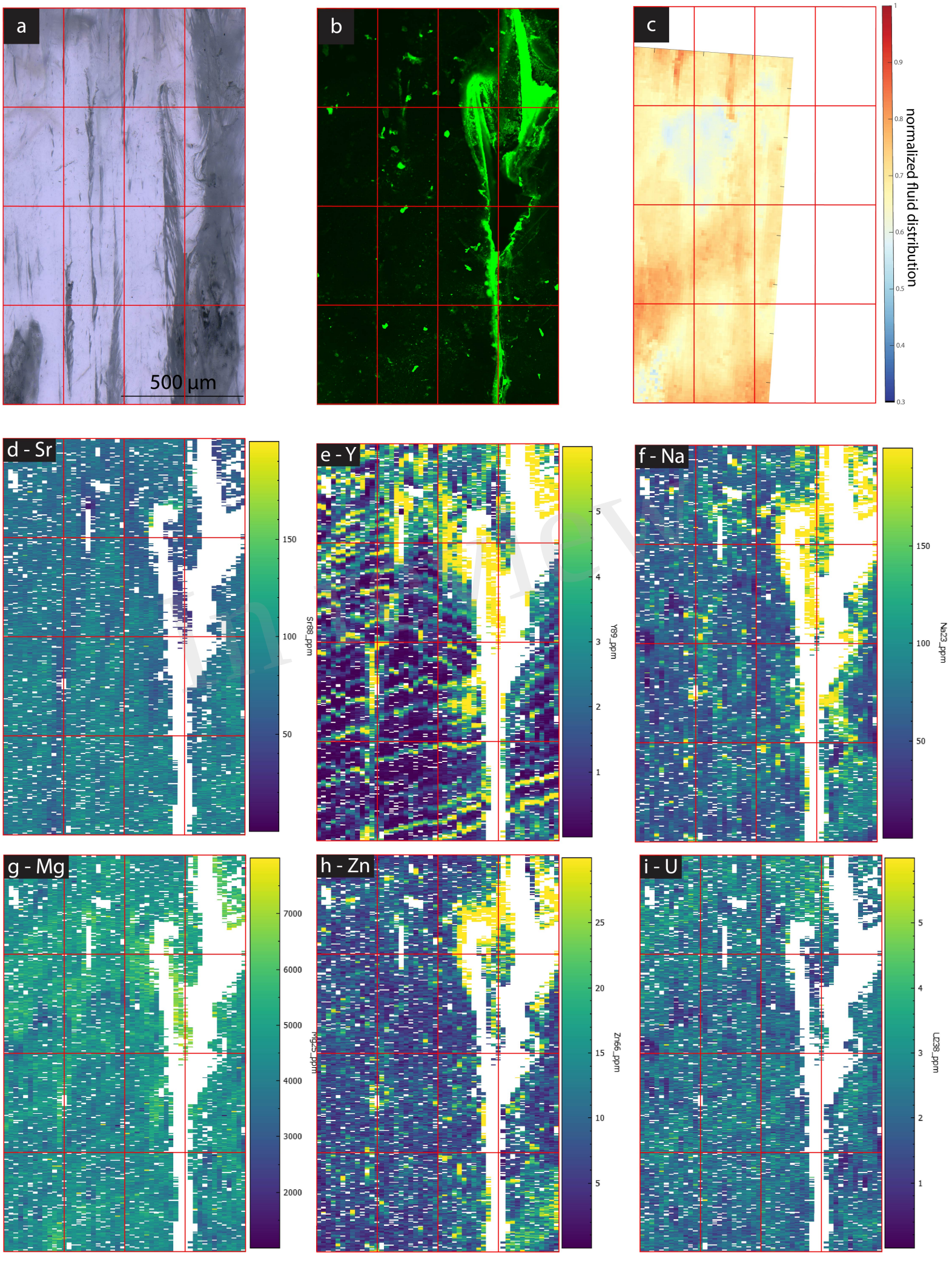

*Supplementary Material*

# The role of Fluid Inclusions and other crystal features affecting trace element distributions in stalagmites

O. Kost[1], J. Sliwinski[2], N. Gies[3], M. Lueder[3], H. Stoll[1*]

*** Correspondence:** Corresponding Author: heather.stoll@erdw.ethz.ch

## 1 Supplementary

### 1.1 Petrographic description of each sample

GLA does not show any visible microscopic layering except the apparent hiatus in the middle of the section marked as a dark brown layer with visible particles (detrital clays and/or organics) (Fig. 1a, b and Fig. S2). Below the hiatus the columnar open calcite ("Co" following the terminology of Frisia, 2015) appears milkier likely due to crystal defects oriented in growth direction. Above the hiatus, the calcite appears very clear and undisturbed by crystal defects (columnar compact calcite, "C"). On a smaller scale, FI's (mostly <10 µm) are often visible and arranged in clouds or clusters. FI clouds are especially prominent around the hiatus (immediately below and above; Fig. S2), as well as near crystal defects. The clear pristine calcite above the hiatus has generally very low FI density. The cross polarized image suggests elongated columnar calcite crystallites assembled in the growth direction. This means, the dense compact calcite is not built by a single crystallite but consists of several small elongated crystallites in the size order of sub- to a few millimeters scale.

MR1 is a complex sample with defects along the growth axis appearing as milky calcite (Fig. 2a, b; Fig. S3). Since the investigated area on MR1 is hosted in a single big crystallite (5-6 mm, as suggested by the cross polarized light microscopy Fig. 2b), the calcite fabric is likely "porous microcrystalline" (Pcm; Chiarini et al., 2017). Horizontal bands of FI's are visible throughout the sample, often appearing elongated and measuring up to 15 µm (Fig. S3). The FI density is generally relatively high compared to GLA and the size of sub-rounded inclusions is on the order of a few micrometers (<8 µm). The FI bands appear slightly darker compared to other samples. It is unclear whether this is due to the higher FI density or if there are submicroscopic particles obscuring the transmitted light. A prominent horizontal crack is observed in the middle of the section, and it is unclear whether this crack already existed before sample preparation or if it was introduced during thick section preparation.

PG2 is a brittle sample with many fine-scaled defects along the growth axis (Fig. 3a, b). Like MR1, the milky texture and lack of multiple crystallites makes this a likely porous microcrystalline (Pcm) texture. It should be noted that a bit further to the left of the investigated area individual crystallites appear under cross-polarized light with only few crystal defects (columnar open calcite, Co). Although few FI's are visible, they are very homogenously distributed. A few striae with slightly higher FI density are observed in growth direction. Some larger pores or crystal defects contain

detrital material (dark particles). But the dense calcite does not contain any visible detrital particles and also does not appear brownish, which would suggest impurities.

SS1 is formed of dense milky calcite with some visible banding along growth layers (Fig. 4a, b). The bands are enriched in elongated FI which can be up to 20 µm in length. Most FI's are in the range of 3- 8 µm (Fig. S4). A fracture appears prominently in the calcite, crosscutting annual layers and the growth axis. It remains unclear whether this is a fossil fracture or a result of sample preparation. No crystal boundaries are detected in the cross polarized image, suggesting a single crystal dominates the region of interest. Despite a few detrital particles in larger pores and defects, the calcite does not appear to contain any impurities. It is best characterized as porous microcrystalline calcite (Pcm).

SS2 derives from the same stalagmite as SS1 (the two investigated areas are < 1 cm apart), however, substantial differences are observed between the two sections. Although the calcite fabric is similar (Pcm), SS2 shows some brownish growth layers with detrital enrichment (Fig. 5a, b). These coincide with layers of high FI density, although FI-rich bands also appear without impurities. Most FI's are in the range of a few micrometers in diameter (2-8 µm). A potential hiatus is detected in the middle of the section manifested by a dark appearance and a high density of elongated FI's with a length of up to >50 µm (Fig. 5 quadrants A2-B2; Fig. S5). Below the hiatus the FI density is generally lower and no bands are detected. However, crystal defects in the growth direction are observed, which can contain some detrital particles. A prominent fracture along a crystal boundary (cross polarized image) is visible (Fig. 5 quadrant A1-A4). Most of the investigated area is situated on a single crystal (>5 mm long and ca. 3 mm wide) but covers this crystal boundary and part of the neighboring crystallite. Across the vertical fracture another crystallite is covered.

### 1.2 Quantification of water content impact on measured Na, Mg, and Sr

Given the quantitative estimates of water fraction (Supplementary Figure S4) it is possible to assess how this magnitude of water might affect the bulk elemental composition and its spatial variation. We carry out estimations assuming this estimate represents water, but if a fraction represents OH groups then we will overestimate the influence of water on the geochemistry.

We use the average LA-measured element concentration for each sample to constrain possible scenarios for the contribution of calcite and water-hosted trace element concentration in that sample. For the actively growing stalagmites, we employ the dripwater chemistry determined from monitoring study(Kost et al., accepted), and for GLA we employ the dripwater chemistry of PG1, which has the most similar Mg/Ca range to GLA. Two less constrained factors in the calculation are the actual yield of water intercepted in the upper 10 microns of LA depth, and the water-free calcite partitioning coefficient for the element in the stalagmite. Because the quantitative estimates of water is made over an integrated 500 micron thickness, the content in the upper 10 microns may be lower if inclusions are disrupted during sample preparation. To account for the possibility that the intercepted water content is proportional to but lower than the average water content, we explore possible yields which may be two-fold lower than the average water content. This is a sensitivity analysis and other factors of reduction are also possible. To set the water-free calcite partitioning coefficient, we use the range of Na partitioning coefficients from (Fuger et al., 2019) It is uncertain if water is present in laboratory grown calcites. No water has been described; the reduced detrital and dissolved organic components compared to dripwater may make such experimental crystals less likely to host defects and water, although they are characterized by rapid growth rates which may enhance defects in some systems. For each stalagmite, we select a Na partitioning coefficient within the published range

which provides greatest coherence to observed mean measured Na concentration. To set the water-free calcite partitioning coefficient for Sr and Mg, we begin with the bulk partioning coefficient illustrated in Figure 9, and iteratively adjust it so that the calcite plus water bulk partitioning matches the observed laser ablation mean. We do not propose that this is a unique nor exhaustive solution to the effect of water on elemental ratios, but an example analysis of the effect of the spatial range of water content on the variability of Na, Mg, and Sr concentration in the measured samples.

For SS, the mean measured Na concentration can be simulated with calcite partitioning coefficients in the highest range of laboratory estimates (Fuger et al., 2019) and assuming the yield of water in the laser ablated area is identical to that measured through the sample by FTIR (Table S1, simulation series SS-A). For these parameter choices, the range of water observed in SS would be expected to yield >2-fold spatial variations in Na concentration correlating with the range of calculated water content. In contrast, we do not observe that high Na regions coincide with high water regions in SS1 or SS2. A similar Na concentration of the sample but no large spatial variations in Na concentration correlated with water content, could be simulated with a nearly 3-fold higher Na partitioning in the calcite, and assuming a 2-fold lower water yield in the upper 10 μm surface sampled by laser ablation (Table S1, simulation series SS-B). The higher effective Na partitioning in the calcite could reflect enhancement of Na incorporation by coupled Na-Y substitution. The filtering of LA maps for regions of high Al should limit the contribution of Na present in aluminosilicates to the mean signal. For SS, the simulated spatial variation in water content would lead to 4% to 2% spatial variation in Mg concentration in SS-A and SS-B scenarios, respectively, and <1% spatial variation in Sr concentration.

For MR1 and PG2, the mean measured Na concentration can be simulated with calcite partitioning coefficients in the lowest range of laboratory estimates (Fuger et al., 2019) and assuming the yield of water in the laser ablated area is 2-fold lower than that measured through the sample by FTIR (Table S1, simulation series MR and PG). With these parameters, the minimum estimated water content effectively simulates the average Na concentration in MR, but given the typical water abundance, simulation of the average Na concentration overall would require even lower partitioning coefficients or yield of water in the upper 10 μm surface sampled by laser ablation. For PG, these parameters simulate the observed Na concentration for the typical background water content. Spatial variations in Na concentration of 2- to 3-fold are predicted from the range in water content in PG2 and MR1, respectively. Given this set of parameters, the impact of water variations in Mg concentrations is larger in MR1 (estimated as 5%) compared to PG2 (2%) due to the higher DMg estimated for PG2. Varying water content induces <1% variation in Sr concentrations in these stalagmites.

Assuming that modern PG2 dripwater is representative for GLA, simulation of the mean Na concentration would require even lower partitioning coefficients and/or lower yield of water in the upper 10 μm surface sampled by laser ablation, compared to parameters used to simulate PG2 and MR1 (Table S1, simulation series GLA).

For samples similar to those studied here, our analysis suggests that variations in water content can lead to significant variations in Na concentrations measured by laser ablation in samples with low Na incorporation into calcite, but only limited variations in Mg concentration, and negligible variations in Sr concentration.

## 2 Supplementary Figures

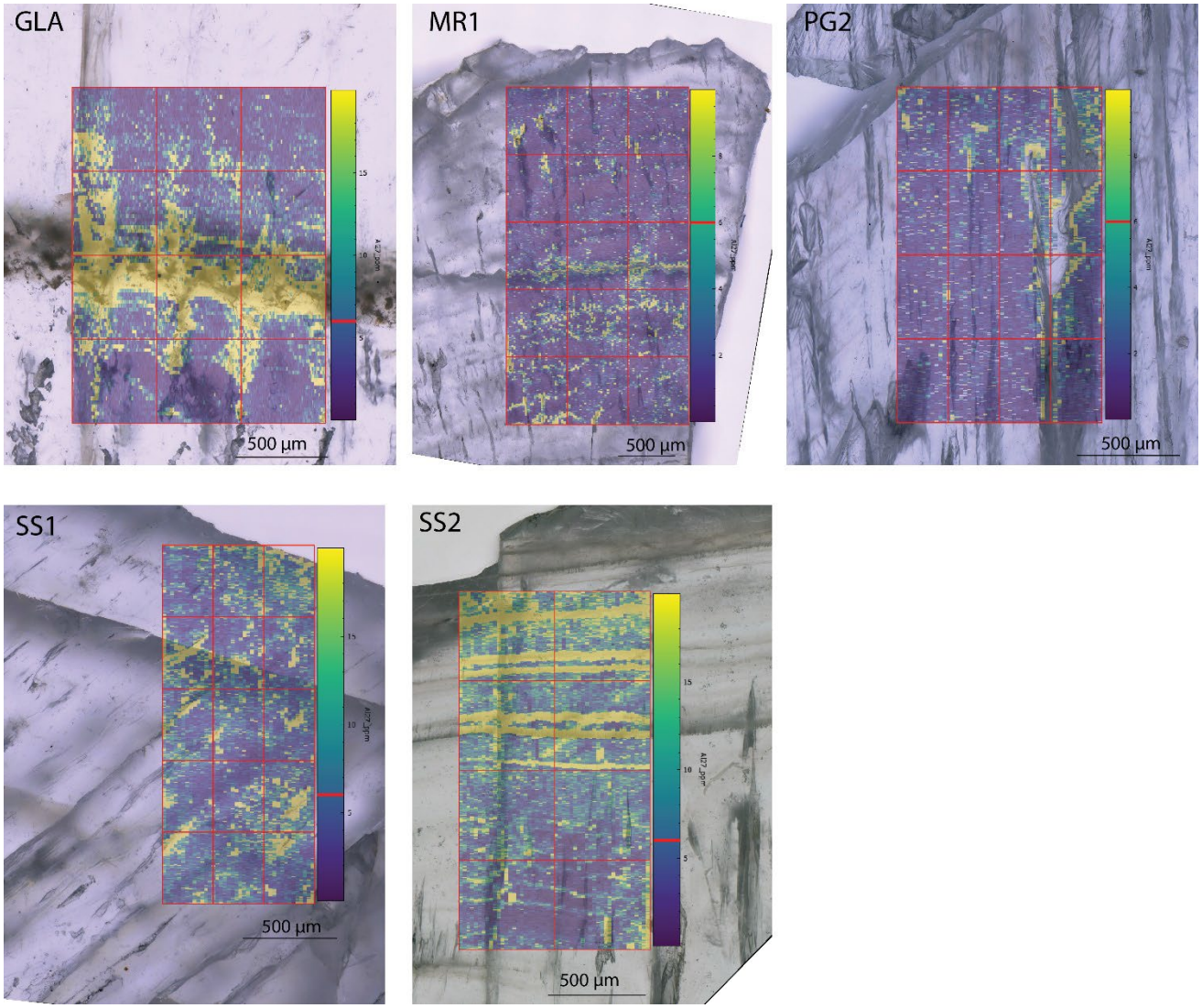


**Supplementary Figure S1.** A map showing the unfiltered Al in all samples on top of the TL image to support results 3.3. The red bar at 6 ppm Al represents the threshold for the detrital filter applied to element maps in the main figures. Missing data (e.g. PG2) occurs due to an applied filter for Ca counts to avoid pores.

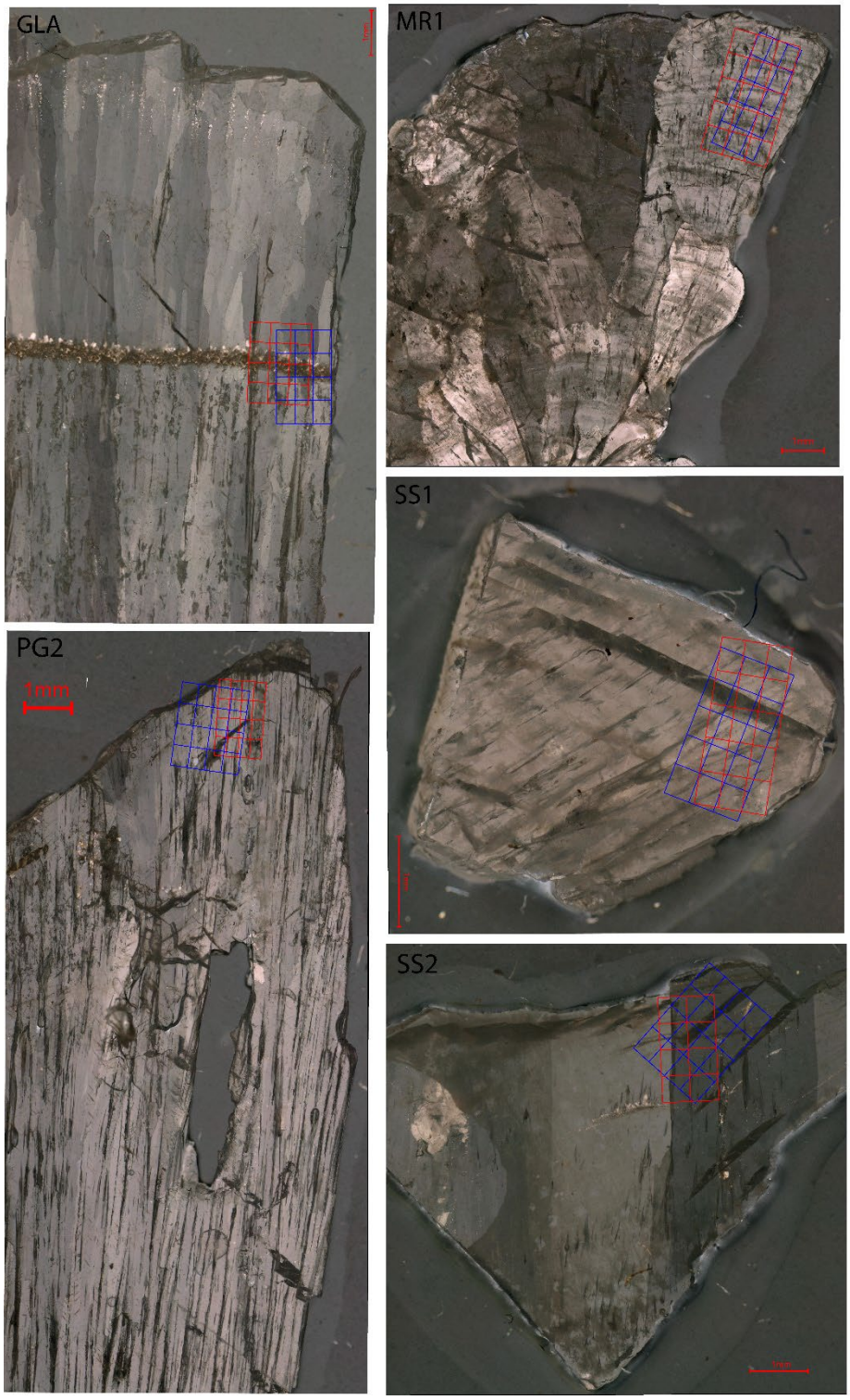


**Supplementary Figure S2.** Full cross polarized transmitted light images of all samples with investigated areas (blue and red grids). The red bar marks 1 mm length scale.

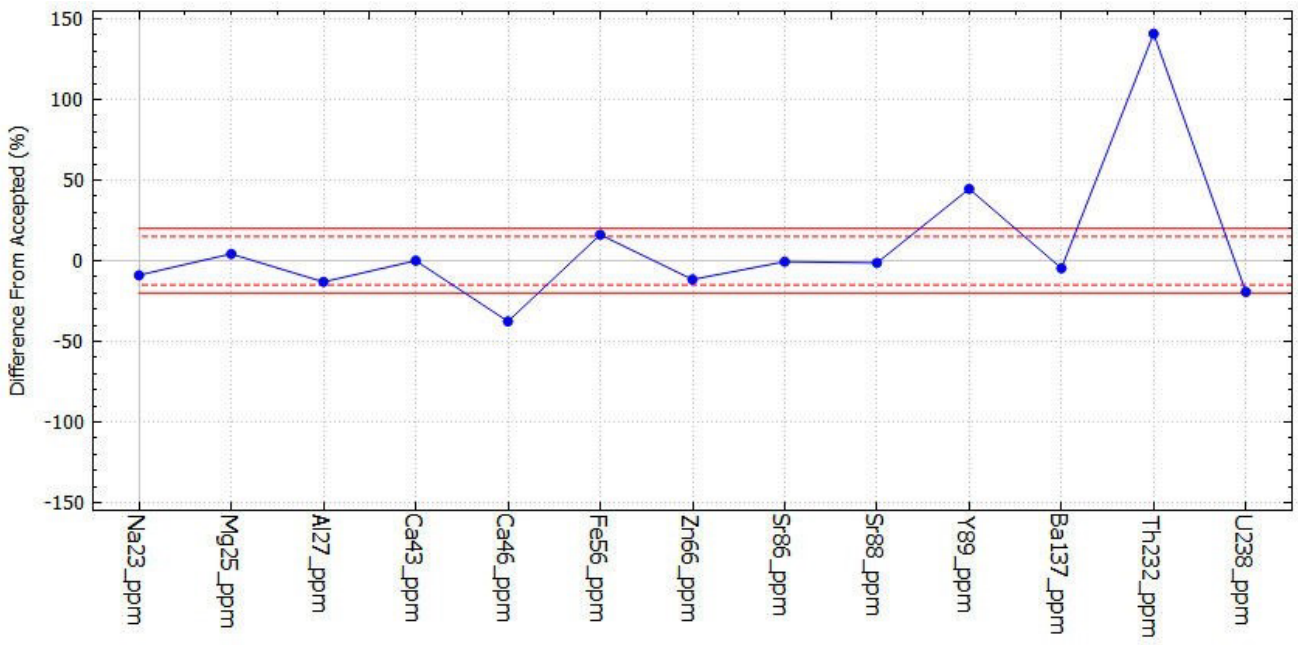


**Supplementary Figure S3.** Example of quality check analysis showing pressed powder standard ECRM. Most elements are well within accepted error. Yttrium may be biased toward too high values. However, the systematic Y offset in ECRM suggests an issue with the reference value provided by µ-standards since other pressed powder standards show no bias in Y but problems with other elements like Sr in the JCt standard for example. Consequently we employ NIST 612 as reference material since this is a well-established standard, while acknowledging typical limitations due to matrix mismatch and variability among different reference standards.

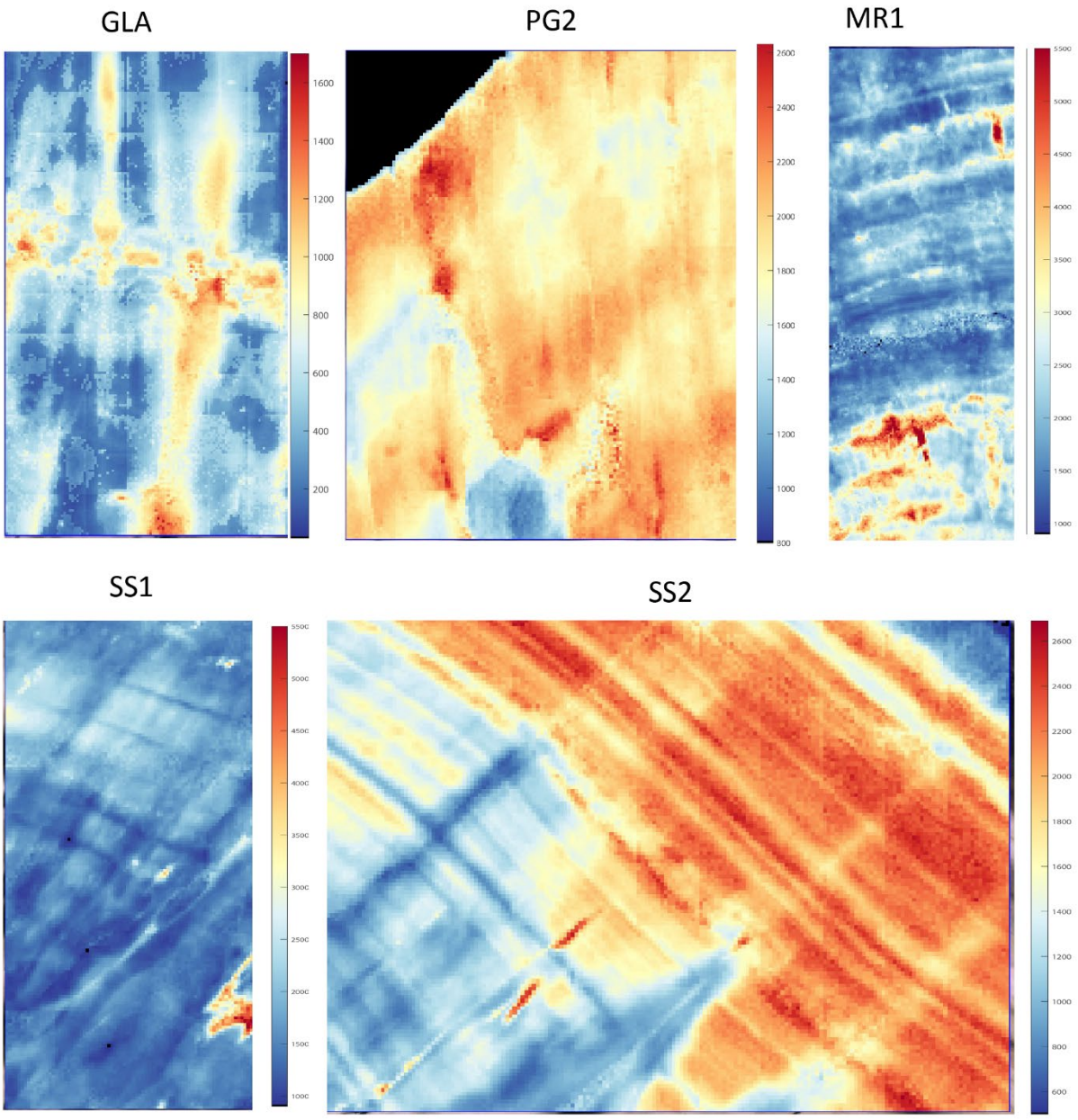


**Supplementary Figure S4.** Maps of water content based on the FTIR 3400 $cm^{-1}$ absorbance peak, applying quantitative, wavenumber specific calibration as described in methods. Imaged area in each sample is identical to Figure 7. Scale bar shows water content in in µg/g (ppm $H_2O$), so 5000 ppm would be 0.5 wt.%.

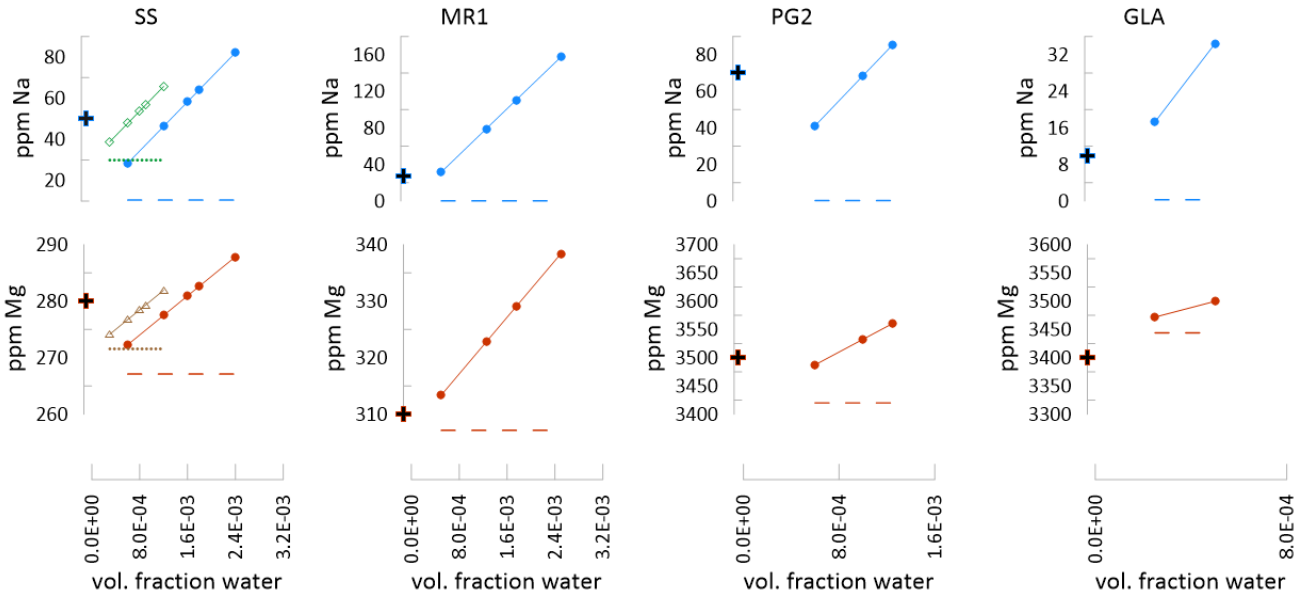


**Supplementary Figure S5.** Simulations of the trace element concentration of stalagmites for a given water content, as calculated in Table S1 and described in Supplementary text section 1.2. The dashed lines indicate the simulated trace element concentration in water-free calcite, and the solid lines with symbols simulates the total trace element concentration in calcite and water phases, assuming water composition identical to modern dripwaters. The cross indicates the mean concentration of the element in the sample. For SS, series SS-A is illustrated by circular symbols with blue and red lines in Na and Mg, respectively. Series SS-B is illustrated by triangular symbols with green and brown lines in Na and Mg, respectively.

## 3 Supplementary Table

| sample | simulation series | scenario | water by volume | DNa water-free calcite | DSr water-free calcite | DMg water-free calcite | -fold reduction of water in upper 10 µm | water yield in upper 10 µm by volume | Na water-free calcite (ppm) | Na calcite+water (ppm) | Sr water-free calcite (ppm) | Sr calcite +water (ppm) | Mg water-free calcite (ppm) | Mg calcite + water (ppm) | mean LA Na (ppm) | mean LA Mg (ppm) | mean LA Sr (ppm) | mean dripwater Na(ppm) | mean dripwater Ca (ppm) | mean dripwater Mg (ppm) | mean dripwater Sr (ppm) |
|---|---|---|---|---|---|---|---|---|---|---|---|---|---|---|---|---|---|---|---|---|---|
| SS | SS-A | SS2 min | 0.060% | 3.50E-04 | 0.075 | 0.030 | 1 | 0.060% | 10.5 | 28 | 30 | 30 | 267 | 272 | 50 | 280 | 31 | 4.25 | 57.0 | 1.25 | 0.057 |
| SS | SS-A | SS2 low range | 0.120% | 3.50E-04 | 0.075 | 0.030 | 1 | 0.120% | 10.5 | 46 | 30 | 31 | 267 | 277 | | | | | | | |
| SS | SS-A | SS2 midvrange | 0.160% | 3.50E-04 | 0.075 | 0.030 | 1 | 0.160% | 10.5 | 58 | 30 | 31 | 267 | 281 | | | | | | | |
| SS | SS-A | SS2 high range | 0.180% | 3.50E-04 | 0.075 | 0.030 | 1 | 0.180% | 10.5 | 64 | 30 | 31 | 267 | 283 | | | | | | | |
| SS | SS-A | SS2 max | 0.240% | 3.50E-04 | 0.075 | 0.030 | 1 | 0.240% | 10.5 | 82 | 30 | 31 | 267 | 288 | | | | | | | |
| | | | | | | | | | | | | | | | | | | | | | |
| SS | SS-B | SS2 min | 0.060% | 1.00E-03 | 0.075 | 0.031 | 2 | 0.030% | 29.9 | 39 | 30 | 30 | 272 | 274 | 50 | 280 | 31 | 4.25 | 57.0 | 1.25 | 0.057 |
| SS | SS-B | SS2 low range | 0.120% | 1.00E-03 | 0.075 | 0.031 | 2 | 0.060% | 29.9 | 48 | 30 | 30 | 272 | 277 | | | | | | | |
| SS | SS-B | SS2 midvrange | 0.160% | 1.00E-03 | 0.075 | 0.031 | 2 | 0.080% | 29.9 | 54 | 30 | 30 | 272 | 278 | | | | | | | |
| SS | SS-B | SS2 high range | 0.180% | 1.00E-03 | 0.075 | 0.031 | 2 | 0.090% | 29.9 | 57 | 30 | 30 | 272 | 279 | | | | | | | |
| SS | SS-B | SS2 max | 0.240% | 1.00E-03 | 0.075 | 0.031 | 2 | 0.120% | 29.9 | 66 | 30 | 31 | 272 | 282 | | | | | | | |
| | | | | | | | | | | | | | | | | | | | | | |
| MR1 | MR | MR min | 0.100% | 4.00E-06 | 0.082 | 0.024 | 2 | 0.050% | 0.3 | 32 | 35 | 35 | 307 | 313 | 27 | 310 | 35 | 8.82 | 56.2 | 1.77 | 0.059 |
| MR1 | MR | MR background | 0.250% | 4.00E-06 | 0.082 | 0.024 | 2 | 0.125% | 0.3 | 79 | 35 | 35 | 307 | 323 | | | | | | | |
| MR1 | MR | MR water rich layers | 0.350% | 4.00E-06 | 0.082 | 0.024 | 2 | 0.175% | 0.3 | 110 | 35 | 35 | 307 | 329 | | | | | | | |
| MR1 | MR | MR pores | 0.500% | 4.00E-06 | 0.082 | 0.024 | 2 | 0.250% | 0.3 | 158 | 35 | 36 | 307 | 338 | | | | | | | |
| PG2 | PG | PG min | 0.120% | 4.00E-06 | 0.11 | 0.030 | 2 | 0.060% | 0.3 | 41 | 80 | 81 | 3420 | 3488 | 70 | 3500 | 80 | 7.31 | 42.9 | 12.25 | 0.078 |
| PG2 | PG | PG background | 0.200% | 4.00E-06 | 0.11 | 0.030 | 2 | 0.100% | 0.3 | 69 | 80 | 81 | 3420 | 3533 | | | | | | | |
| PG2 | PG | PG max | 0.250% | 4.00E-06 | 0.11 | 0.030 | 2 | 0.125% | 0.3 | 86 | 80 | 81 | 3420 | 3561 | | | | | | | |
| | | | | | | | | | | | | | | | | | | | | | |
| GLA | GLA | GLA min | 0.050% | 4.00E-06 | 0.042 | 0.030 | 2 | 0.025% | 0.3 | 17 | 31 | 31 | 3444 | 3472 | 10 | 3400 | 31 | 7.31 | 42.9 | 12.13 | 0.078 |
| GLA | GLA | GLA max | 0.100% | 4.00E-06 | 0.042 | 0.030 | 2 | 0.050% | 0.3 | 34 | 31 | 31 | 3444 | 3500 | | | | | | | |

Supplementary Table 1. Estimations of the effect of water content on the LA-ICPMS measured concentrations of trace elements Na, Mg, and Sr, as described in Supplementary section 1.2. Blue text highlights the scenarios yielding a Na concentration in the range of the observed mean Na concentration for that sample.


Füger, A., Konrad, F., Leis, A., Dietzel, M., and Mavromatis, V.: Effect of growth rate and pH on lithium incorporation in calcite, Geochimica et Cosmochimica Acta, 248, 14-24, 2019.

Kost, O., González-Lemos, S., Rodriguez-Rodriguez, L., Sliwinski, J., Endres, L., Haghipour, N., and Stoll, H.: Relationship of seasonal variations in drip water δ 13 C DIC, δ 18 O and trace elements with surface and physical cave conditions of La Vallina Cave, NW Spain, Hydrology and Earth System Sciences 1-42, accepted.